Center for Environmentally Sustainable Transportation in Cold Climates

A Novel Systematic Strategy Towards Air-Purifying, Corrosion Resistant and Self-Healing Concrete Infrastructure

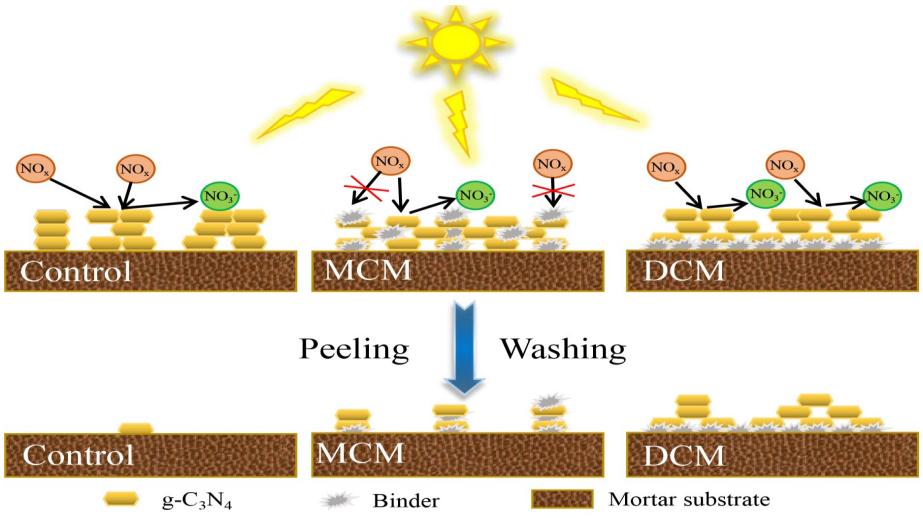

Zhengxian Yang, Ph.D.
Department of Civil & Environmental Engineering
Washington State University

Date: 15/09/2019

Prepared by: Zhengxian Yang, Ph.D.

Center for Environmentally Sustainable Transportation in Cold Climates
University of Alaska Fairbanks
P.O. Box 755900
Fairbanks, AK 99775

U.S. Department of Transportation
1200 New Jersey Avenue, SE
Washington, DC 20590

INE/CESTiCC 19.23

REPORT DOCUMENTATION PAGE

Form approved OMB No.

1. AGENCY USE ONLY (LEAVE BLANK)	2. REPORT DATE	3. REPORT TYPE AND DATES COVERED
	09/2019	Final Report: 09/2016 – 09/2019

4. TITLE AND SUBTITLE

A novel systematic strategy towards air-purifying, corrosion resistant and self-healing concrete infrastructure

5. FUNDING NUMBERS

6. AUTHOR(S)

Name, Title, Organization/University

Zhengxian Yang, Ph.D., Washington State University

7. PERFORMING ORGANIZATION NAME(S) AND ADDRESS(ES)

Center for Environmentally Sustainable Transportation in Cold Climates
University of Alaska Fairbanks
Duckering Building Room 245
P.O. Box 755900
Fairbanks, AK 99775-5900

8. PERFORMING ORGANIZATION REPORT NUMBER

INE/CESTiCC 19.23

9. SPONSORING/MONITORING AGENCY NAME(S) AND ADDRESS(ES)

U.S. Department of Transportation
1200 New Jersey Avenue, SE
Washington, DC 20590

10. SPONSORING/MONITORING AGENCY REPORT NUMBER

11. SUPPLENMENTARY NOTES

12a. DISTRIBUTION / AVAILABILITY STATEMENT

No restrictions

12b. DISTRIBUTION CODE

13. ABSTRACT (Maximum 200 words)

Transportation causes major emissions of harmful gases (NO_x, CO, VOCs). These pollutants also travel long distances to produce secondary pollution such as acid rain. The most popularly used photocatalytic cementitious composites based on TiO_2 achieve the air purification function under ultraviolet sunlight, significantly impeding a broader application of photocatalytic cementitious composites. This study focused on developing an environmentally friendly and durable cementitious system based on the multifunctional photocatalytic Graphitic carbon nitride (g-C_3N_4). The photocatalytic cementitious composites (PCC) were prepared in three manners: (1) incorporating g-C_3N_4 nanosheets (CNNs) in cement at three mixing dosages (0.5%, 1% and 2% by weight of cement), (2) applying CNNs at various concentration levels as the coating on recycled asphalt pavement aggregate, (3) applying CCNs s with vinyl chloride/vinyl ester/ethylene copolymer (as a binder) as the coating on cement mortar. The photocatalytic performance and durability of the newly developed cementitious composites were evaluated systematically and the results showed that the PCC hold marked efficiency in terms of NO_x removal and self-cleaning when the CNNs were applied in a proper way. The obtained knowledge sheds light on a future perspective of developing a novel systematic strategy towards air-purifying, corrosion resistant, and self-healing concrete infrastructure.

14- KEYWORDS:

Photocatalytic cementitious materials; g-C_3N_4 nanosheets; air purification; self-cleaning; recycled asphalt pavement aggregate

15. NUMBER OF PAGES

98

16. PRICE CODE

N/A

17. SECURITY CLASSIFICATION OF REPORT	18. SECURITY CLASSIFICATION OF THIS PAGE	19. SECURITY CLASSIFICATION OF ABSTRACT	20. LIMITATION OF ABSTRACT
Unclassified	Unclassified	Unclassified	N/A

A NOVEL SYSTEMATIC STRATEGY TOWARDS AIR-PURIFYING, CORROSION RESISTANT AND SELF-HEALING CONCRETE INFRASTRUCTURE

FINAL REPORT

by

Zhengxian Yang, Ph.D.
Department of Civil and Environmental Engineering
Washington State University
Pullman, WA 99164

INE/CESTiCC 19.23

September 2019

DISCLAIMER

This document is disseminated under the sponsorship of the U. S. Department of Transportation in the interest of information exchange. The U.S. Government assumes no liability for the use of the information contained in this document. The U.S. Government does not endorse products or manufacturers. Trademarks or manufacturers' names appear in this report only because they are considered essential to the objective of the document.

Opinions and conclusions expressed or implied in the report are those of the author(s). They are not necessarily those of the funding agencies.

METRIC (SI*) CONVERSION FACTORS

APPROXIMATE CONVERSIONS TO SI UNITS

Symbol	When You Know	Multiply By	To Find	Symbol
		LENGTH		
in	inches	25.4		mm
ft	feet	0.3048		m
yd	yards	0.914		m
mi	Miles (statute)	1.61		km
		AREA		
in^2	square inches	645.2	millimeters squared	cm^2
ft^2	square feet	0.0929	meters squared	m^2
yd^2	square yards	0.836	meters squared	m^2
mi^2	square miles	2.59	kilometers squared	km^2
ac	acres	0.4046	hectares	ha
		MASS (weight)		
oz	Ounces (avdp)	28.35	grams	g
lb	Pounds (avdp)	0.454	kilograms	kg
T	Short tons (2000 lb)	0.907	megagrams	mg
		VOLUME		
fl oz	fluid ounces (US)	29.57	milliliters	mL
gal	Gallons (liq)	3.785	liters	liters
ft^3	cubic feet	0.0283	meters cubed	m^3
yd^3	cubic yards	0.765	meters cubed	m^3
		TEMPERATURE (exact)		
ºF	Fahrenheit temperature	5/9 (ºF-32)	Celsius temperature	ºC
		ILLUMINATION		
fc	Foot-candles	10.76	lux	lx
fl	foot-lamberts	3.426	candela/m^2	cd/cm^2
		FORCE and PRESSURE or STRESS		
lbf	pound-force	4.45	newtons	N
psi	pound-force per square inch	6.89	kilopascals	kPa

Note: Volumes greater than 1000 L shall be shown in m^3

These factors conform to the requirement of FHWA Order 5190.1A *SI is the symbol for the International System of Measurements

APPROXIMATE CONVERSIONS FROM SI UNITS

Symbol	When You Know	Multiply By	To Find	Symbol
		LENGTH		
mm	millimeters	0.039	inches	in
m	meters	3.28	feet	ft
m	meters	1.09	yards	yd
km	kilometers	0.621	Miles (statute)	mi
		AREA		
mm^2	millimeters squared	0.0016	square inches	in^2 m^2
meters squared		10.764	square feet	ft^2 km^2
kilometers squared		0.39	square miles	mi^2 ha
hectares (10,000 m^2)		2.471	acres	ac
		MASS (weight)		
g	grams	0.0353	Ounces (avdp)	oz
kg	kilograms	2.205	Pounds (avdp)	lb mg
megagrams (1000 kg)		1.103	short tons	T
		VOLUME		
mL	milliliters	0.034	fluid ounces (US)	fl oz
liters	liters	0.264	Gallons (liq)	gal
m^3	meters cubed	35.315	cubic feet	ft^3
m^3	meters cubed	1.308	cubic yards	yd^3
		TEMPERATURE (exact)		
ºC	Celsius temperature	9/5 ºC+32	Fahrenheit temperature	ºF
		ILLUMINATION		
lx	lux	0.0929	foot-candles	fc
cd/cm^2	candela/m^2	0.2919	foot-lamberts	fl
		FORCE and PRESSURE or STRESS		
N	newtons	0.225	pound-force	lbf
kPa	kilopascals	0.145	pound-force per square inch	psi

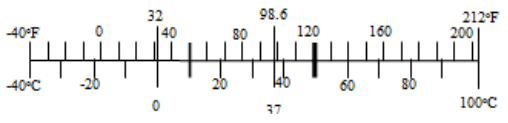

ACKNOWLEDGMENTS

The author wishes to express sincere appreciation to the Center for Environmentally Sustainable Transportation in Cold Climates (CESTiCC) for its support on this study. Acknowledgment extended to the Natural Science Foundation of Fujian Province, China (2019J01235) and Minjiang scholar program of Fujian province (XRC-19045) for partial support for this study. The author would also like to thank Dr. Yong Zhang and Yu Yang at the Fuzhou University of China for their assistance in this project.

TABLE OF CONTENTS

LIST OF FIGURES

LIST OF TABLES

EXECUTIVE SUMMARY

The combination of photocatalysts with cementitious materials for air pollution abatement and self-cleaning has gained considerable attention. However, the most popularly used photocatalytic cementitious composites based on TiO_2 achieve the purification function under ultraviolet sunlight, significantly impeding a broader application of photocatalytic cementitious composites. In this context, this study focused on developing an environmentally friendly and durable cementitious system based on synergistic activities of multifunctional photocatalytic Graphitic carbon nitride (g-C_3N_4).

The photocatalytic cementitious composites (PCC) were prepared in three manners:

(1) Incorporating g-C_3N_4 nanosheets (CNNs) in Portland cement at three mixing dosages (0.5%, 1% and 2% by weight of cement).

(2) Applying CNNs suspension at various concentration levels as the coating on recycled asphalt pavement aggregate (RAPA).

(3) Applying CCNs suspension with vinyl chloride/vinyl ester/ethylene copolymer (as a binder) as the coating on cement mortar.

The photocatalytic performance and durability of the newly developed photocatalytic cementitious composites were evaluated systematically and the results showed that the PCC indeed hold marked efficiency in terms of NO_x removal and self-cleaning when the CNNs were applied in a proper way. While this work mainly showcases the photocatalytic behavior and durability of the cementitious composites with CNNs, the obtained knowledge sheds light on future possibilities to developing a novel systematic strategy towards air-purifying, corrosion resistant, and self-healing concrete infrastructure.

CHAPTER 1 INTRODUCTION

1.1 Problem Statement

The US has the world's largest transportation system, including 6.3 million kilometers of streets, roads, and highways, as well as numerous bridges and tunnels. While the importance of the national transportation network is well established, high traffic volume causes major emissions of harmful gases (NO_x, CO) and volatile organic compounds (VOCs) into the air. These pollutants carry significant risks for public health and account for around 30% of the United States' total contribution to global warming pollution. These pollutants also travel long distances to produce secondary pollution such as acid rain, threatening the durability of concrete infrastructure and vegetation in rural areas. A promising solution lies in the utilization of semiconductor-based photocatalysis driven by inexhaustible and clean solar energy [1, 2]. As illustrated in Figure 1.1, by exposing the photocatalyst to solar light, the electrons (e^-) in the valence band transfer to the conduction band leaving holes (h^+). The e^- and h^+ can reach the surface of the semiconductor particle initiating the redox process. The e^- of the conduction band with strong reducing potential reacts with oxygen to produce superoxide radicals ($\bullet O_2^-$). Then the $\bullet O_2^-$ reacts with water molecules to form the hydroxyl radicals (•OH). The generated h^+ reacts with hydroxyl groups from water molecules, surrounding the photocatalyst, to form •OH. Afterwards, the •OH acts as a strong oxidant with the potential to decompose a wide range of air pollutants (VOCs, NO_x, etc.) [3, 4]. However, these semiconductor-based photocatalysts are usually powdery. In order to ensure photocatalytic performance, nano-sized photocatalytic

materials are often immobilized onto a supporting material or substrate to prevent loss from mechanical abrasion and environmental damages.

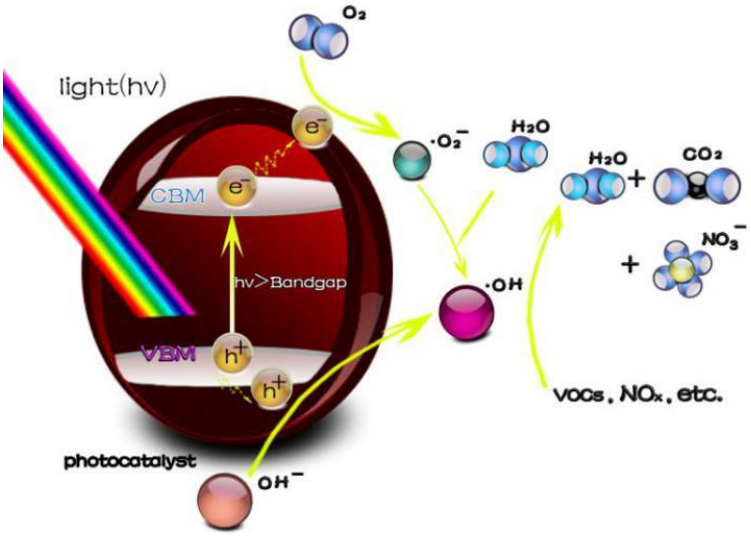

Figure 1.1 Schematic illustration of the mechanism for photodegradation of the air pollutants.

Due to their inherent porous nature, cementitious materials are the potential substrate for the application of photocatalytic materials in building and construction industries. The surfaces of urban construction are typically exposed to the highest levels of air pollution. Photocatalysis on building materials is an attractive sustainable strategy to purify air pollutants and endow the building with self-cleaning and antimicrobial properties [5, 6]. The photocatalytic cementitious materials used have been fabricated using various preparation methods, such as spray coating and intermixing. Martinez et al. applied a polymer-matrix-based coating incorporating nano-TiO_2 to the different substrates and found that the use of mortar as the substrate showed the best photocatalytic performance of degradation of NO [7]. Ângelo et al. reported a highly active photocatalytic paint incorporated with TiO_2 for outdoor NO_x abatement [8]. Guo et al. studied a TiO_2-intermixed concrete surface layer with good photocatalytic NO removal ability and found

that harsh abrasion exerted no obvious deterioration to photocatalytic performance of TiO_2-intermixed cementitious materials [9]. The photocatalytic coatings on building materials often exhibit a weak adhesion to the substrates, causing poor durability in aggressive outdoor environments [10]. In contrast, intermixing photocatalyst with cementitious materials is an easy and universal method for preparing photocatalytic cementitious composites, which harbor robust resistance to abrasion action and weathering in real-life service [9].

At present, titanium dioxide (TiO_2) is the most commonly used photo-catalyst due to its chemical stability and high reactivity. Thanks to its inert nature and ease of use, TiO_2 has been widely incorporated in building materials to improve the aesthetics and hygiene of urban infrastructures and to combat the urban air pollution [11, 12]. However, due to its wide band gap (3.2 eV) TiO_2 can only be excited under UV irradiation to form photogenerated electron–hole pairs. It is unfortunate that only about 4.5% of the solar spectrum falls in the UV range [13]. This adversely impedes a broader application of TiO_2. Moreover, TiO_2 was recently reported for the possibility of causing cancer when inhaled [14]. Therefore, the development of nontoxic photocatalysts with an outstanding visible light activity for use in building materials is imperative.

Further concern exists in concrete exposed to atmospheric pollutants and/or deicing salts in cold regions, which presents a high risk of rebar corrosion and cracking. Chloride (mainly from deicing salts and seawater) induced corrosion is a major threat to the durability of concrete structures. Once corrosion initiates, three main consequences occur: (1) local pitting corrosion of the reinforcement; (2) cracking and spalling of the concrete cover due to build-up of voluminous corrosion products; and (3) decrease of ductility and reduction of cross section of the reinforcing

steel. The remediation of concrete bridges in the US, undertaken as a direct result of chloride-induced rebar corrosion, costs US highway departments $5 billion per year [15]. The direct cost of metallic corrosion for highway bridges was estimated at $8.3 billion per year, let alone the indirect costs (traffic delays, lost productivity, etc.) [16]. Another problem is the development of microcracks in cementitious composites as a result of mechanical loadings, environmental loadings (e.g., freezing and thawing, rebar corrosion and chemical attack), and volumetric instability (e.g., shrinkage). Once formed, they are extremely difficult to detect and repair by conventional methods before they develop, coalesce and grow into macrocracks. Obviously, cracking of concrete accelerates the ingress of water, CO_2, chlorides and other deleterious species from automobile emissions. The combination of these activities further undermines the integrity of the structure through aggravated corrosion of the metal inside concrete and eventually leads to the premature failure of concrete infrastructure. In this context, innovative research within the domain of materials science is vitally needed to search for more effective measures to improve the durability of concrete (i.e., corrosion and crack resistance), and to help control air pollution from automobile emissions. Environmentally friendly and durable concrete infrastructure with extended service life is a goal of these efforts.

1.2 Background

To address the critical concerns associated with the use of nano-TiO_2 for removing air pollutants from vehicle emissions, and to improve concrete durability, this project studied a novel systematic strategy towards air purifying, corrosion resistant and self-healing concrete infrastructure. The study involved manipulating cement chemistry and implementing a molecular

immobilization mechanism of Graphitic carbon nitride (g-C_3N_4), within a multifunctional host composite, e.g. Layered Double Hydroxide (LDHs).

LDHs are a group of anionic clay minerals whose structure can be represented by the general formula $[M^{II}_{1-x}M^{III}_x(OH)_2]^{x+}[(A^{n-}_{x/n})]^{x-}\bullet mH_2O$. Here, M^{II} and M^{III} represent di- and trivalent metal cations respectively, which provide positive charges for layers and balance the interlayered anions of A^{n-} and hydration water molecules. LDHs are relatively cheap and easy to produce with the possibility of tailoring their physical and chemical properties during synthesis. Recent studies [17] found that in light of their unique structural properties and high specific surface area (around 20 m^2/g) LDH compounds could be utilized as a host matrix to couple with other nanoparticles for developing highly active photocatalysts. To date, much academic work and commercial interest has been invested in LDHs [18] for corrosion protection of metals. However, little effort has been directed towards cementitious materials in combination with g-C_3N_4, for environmental remediation.

1.3 Objectives

To address the critical concerns associated with air-purifying by nano-TiO_2, the objective of this project was to develop an environmentally friendly and durable cementitious system based on synergistic activities of multifunctional photocatalytic Graphitic carbon nitride (g-C_3N_4) and conduct performance and durability evaluation of the newly developed photocatalytic cementitious composites.

1.4 Scope of the Work

To achieve the objectives of this project, the following investigations occurred:

1) Photocatalytic NO_x abatement and self-cleaning performance of cementitious composites with g-C_3N_4 nanosheets under visible light.
2) Washing resistance of the photocatalytic cementitious materials based on g-C_3N_4 nanosheets-recycled asphalt pavement aggregate composites.
3) Efficiency and durability of g-C_3N_4-based coatings applied on mortar under peeling and washing trials.

CHAPTER 2 PHOTOCATALYTIC NO_X ABATEMENT AND SELF-CLEANING PERFORMANCE OF CEMENTITIOUS COMPOSITES WITH G-C_3N_4 NANOSHEETS UNDER VISIBLE LIGHT

2.1. Introduction

Graphitic carbon nitride (g-C_3N_4), a typical graphite-like layered material, is well known as a nontoxic metal-free semiconductor [19]. With its unique features such as high thermal and chemical stability, high-hardness and visible-light driven band gap, g-C_3N_4 is considered as a kind of prospective photocatalyst in various applications including water splitting [20], CO_2 reduction [21], and pollutants removal [22,23]. Over the past few years, g-C_3N_4 has become a fascinating visible light driven photocatalyst for environmental pollution mitigation. Chang et al. found that the porous g-C_3N_4 prepared by a facile pyrolysis method showed remarkable photocatalytic performance in degradation of Rhodamine B (RhB) under visible-light [24]. Papailias et al. reported that the g-C_3N_4 obtained via thermal polycondensation of melamine could effectively remove NO_x under visible light [25]. Sano et al. found that the photocatalytic NO abatement of g-C_3N_4 under visible light could be significantly improved by 8.6 times compared to the conventional g-C_3N_4 via an alkaline hydrothermal treatment [26]. Compared to inherent wide band gap of TiO_2 (3.2 eV) which is excited only under UV irradiation, g-C_3N_4, owing to its narrow band gap of 2.7 eV, offers a great potential for air purification under visible light. Furthermore, g-C_3N_4 can be synthesized in a large scale with low cost by polycondensation of various carbon and nitrogen-containing organic precursors.

Normally, there are two types of g-C_3N_4: bulk g-C_3N_4 and g-C_3N_4 nanosheets (CNNs). Compared with the bulk g-C_3N_4 prepared by traditional thermal polymerization, ultrathin CNNs

are extremely advantageous for promoting photocatalysis efficiency. The apparent advantages associated with nanosheets include large specific surface area for providing abundant reactive sites and short bulk diffusion length for reducing the recombination probability of photoexcited charge carriers [27,28]. Recently, Kou and co-workers reported a new g-C_3N_4 based photocatalytic cement, showing an enhanced visible-light photocatalytic activity via construction of the SnO_2/g-C_3N_4 heterostructures to enhance electron-hole separation and interfacial charge transfer [29].

This chapter introduces a novel photocatalytic cementitious composite based on CNNs. The researchers examined the photocatalytic performances in terms of NO_x removal in a continuous mode and discoloration of RhB under visible light. Furthermore, the effect of CNNs on microscopic mechanical property of the cementitious materials, cement hydration and composite hydration products were investigated by micro-hardness, isothermal calorimetry, X-ray diffraction (XRD), Fourier transform infrared (FTIR), thermogravimetry (TG) and field emission scanning electron microscopy (FESEM). This chapter provides a theoretical basis for the beneficial use of an earth-abundant g-C_3N_4 photocatalyst as a multifunctional material in sustainable building and constructions for improved environmental pollution mitigation.

2.2 Experimental

2.2.1. Materials

The research used a grade 42.5R Portland cement, which is in accordance with Chinese standard (GB/T17671-1999). The composition of the cement in wt% is as follows: C_3S (tricalcium silicate): 55.6, C_2S (dicalcium silicate): 19.6, C_3A (tricalcium aluminate): 7.5, SO_3 (sulphur trioxide); 2.1, C_4AF (tetracalcium alumino ferrite): 9.3. Melamine, ammonium chloride

and commercial titanium dioxide (TiO_2) were purchased from Sinopharm Chemical Reagent Co. Ltd. and used without further purification. All experiments used deionized water.

2.2.2. Synthesis of g-C_3N_4 nanosheets

Motivated by a previous report [30] and thanks to the gases (NH_3 and HCl) released from NH_4Cl with the increase of temperature, the large-quantity and high-quality few-layer g-C_3N_4 nanosheets (CNNs) were prepared through a one-step method. In a typical procedure, 4 g of melamine powders and 20 g ammonium chloride were fully mixed and heated at 550 ℃ for 4 h with a heating rate of 3℃ min^{-1}. Upon cooling down, the resultant fluffy agglomerates were milled into powders in an agate mortar for further use. The structural features of the as-prepared CNNs were investigated using XRD and FTIR (Figure 2.1). Figure 2.2 (a) shows the morphology of the CNNs, and the ultrathin thickness (approximately 5 nm) was further verified by AFM image (Figures 2.2(b) and (c)). The particle size distribution and nitrogen adsorption–desorption isotherms of the CNNs are shown in Figure 2.3 and Figure 2.4, respectively. The BET surface area of the CNNs is about 76.6 m^2 g^{-1}.

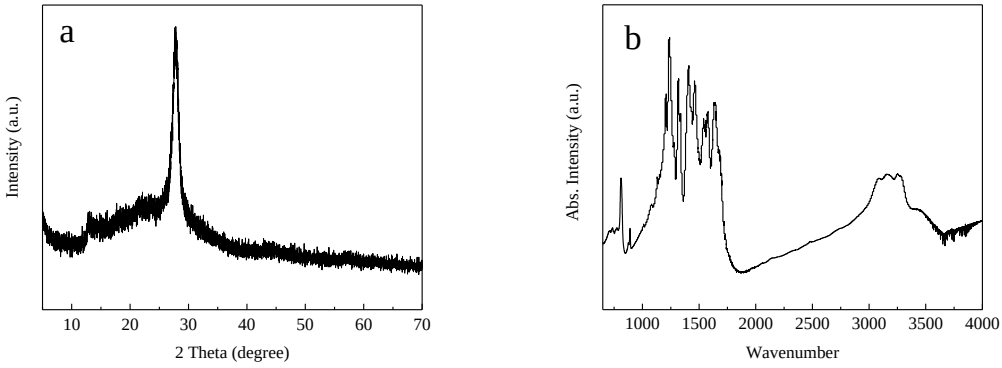

Figure 2.1 (a) XRD patterns and (b) FTIR spectroscopy of CNNs.

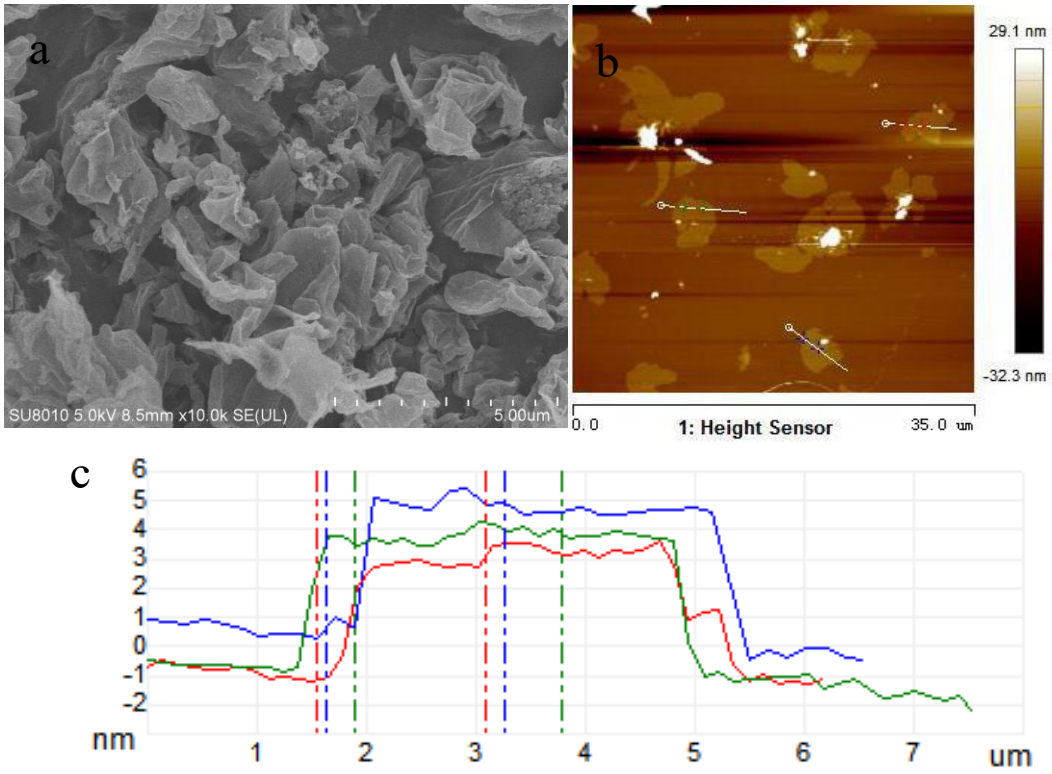

Figure 2.2 (a) FESEM image, (b) AFM image and (c) corresponding cross-sectional profile of CNNs.

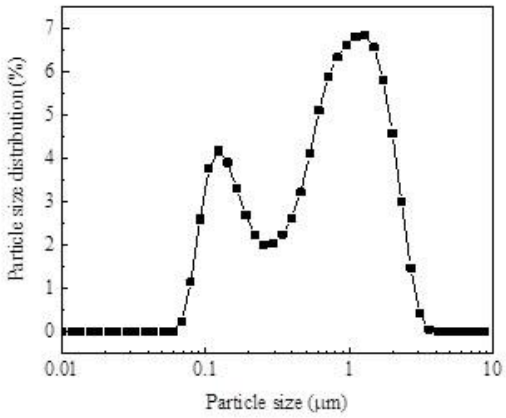

Figure 2.3 Particle size distribution of CNNs.

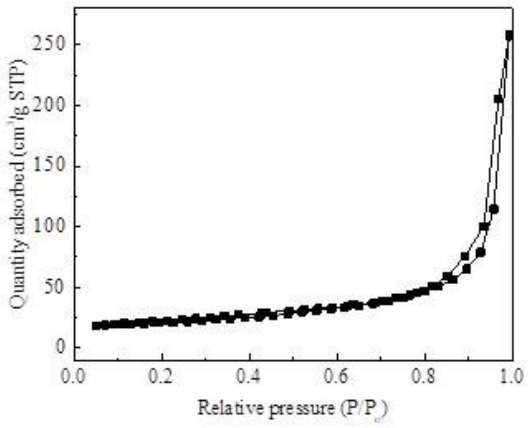

Figure 2.4 Nitrogen adsorption–desorption isotherms of CNNs.

2.2.3. Preparation of photocatalytic cementitious composites

For the preparation of photocatalytic cementitious composites, the water/cement ratio for all batches was kept consistent at 0.4. The CNNs suspensions were prepared first by dispersing the CNNs (0.5, 1 and 2% by the weight of cement) into deionized water for 2 h under ultrasonication. Then ordinary Portland cement and CNNs suspension were mixed in a standard lab mixer for 2 min with a revolution speed of 200 ± 5r min^{-1}, and another 2 min of 300 ± 5 r min^{-1}. After mixing, the fresh cementitious composites were cast into molds (diameter 30 mm, thickness 5 mm) under compaction on a vibration table. The samples were then left in the mold for 24 h before demolding and cured in an environmental chamber at 20 ± 2 ℃ and over 95% relative humidity for 6 additional days before subjecting to assigned tests. As a preliminary exploration of using CNNs in cementitious composites, the effect of CNNs on cement hydration after 7 days was studied. According to previous reports, the compressive strength and the hydration degree of 42.5R Portland cement cementitious composites cured for 7 days can reach 80~95% [31-33] and 75~91% [34], respectively, of that for 28 days, suggesting that the composites have reached a high maturity at a curing age of 7 days. In addition, the 2% TiO_2

added cement composite was prepared as reference sample in test of photocatalytic activity via the foregoing method.

2.2.4. Microscopic hardness

Microscopic hardness is a fast way for measuring the effects of CNNs on the mechanical properties of cementitious composites since it is directly related to the strength of the material [35]. A Vickers Microhardness tester (THVS-1-800 M-AXY) with a load of 0.5 N. determined micro-hardness (HV) of photocatalytic cementitious composites. The sample was ground on an automatic machine using various sand paper with grade of #320, #600, #800, and #1200 sequentially, until a flat mirror surface was obtained. Then the ground sample was cleaned with deionized water and dried in a vacuum oven at 45℃ for 12 h. Statistical tests carried out over each sample ensured a reliable measurement of the local mechanical properties. The indentation was repeated for 30 times on different areas of the sample surface. The interval distance of adjacent vertexes was set as 50 μm.

2.2.5. Phases characterization

The phase compositions of samples were characterized by X-ray diffraction (XRD) analysis on a Bruker D8 Advance X-ray diffractometer with a Cu Kα ray source. Fourier transform infrared (FTIR) spectra were obtained using a Thermo Scientific Nicolet IS50 Fourier transform infrared spectrometer at a resolution of 2 cm^{-1}. Sixty-four scans were performed to obtain each spectrum. Thermogravimetry (TG) analysis of samples was performed using a Netzsch STA449 F3 simultaneous Thermogravimetric analyzer to measure the content of non-evaporable water (NEW) and hydration products in cementitious composites. The non-evaporable water (NEW) content measurement is one of the most intensively used methods for monitoring the degree of cement hydration [36]. The condition of TG analysis was in a nitrogen

atmosphere (flow rate of 80 mL min^{-1}) at a heating rate of 10℃ min^{-1} up to 1000℃. The morphology of the materials was observed by a Thermoscientific Verios G4 UC field emission scanning electron microscope (FESEM). A tapping-mode atomic force microscopy (AFM, Dimension Icon, Bruker) with Si-tip cantilever was used to probe the thickness of the synthesized CNNs on the mica substrate. The hydration heat of cementitious composites was measured by a TAM air isothermal microcalorimeter (TA Instruments, USA). The measurement of hydration heat was performed at an isothermal condition (25 ± 0.1°C). The 5 g of Portland cement was first put into a sample ampoule of thermometric TAM. The as-prepared CNNs suspension was added to the sample ampoule with a syringe. Afterwards, the paste was mixed with a special electric stirrer for 90 s and placed into the chamber of TAM Air. The hydration heat evolution rate and cumulative hydration heat of the cementitious composites containing CNNs can be monitored as a function of time. The water/cement ratio (0.4) used was the same as to prepare the photocatalytic cementitious composites mentioned above.

2.2.6. Visible light photocatalytic activity

2.2.6.1. Visible light photocatalytic removal of NO_x in air

The photocatalytic NO_x abatement of the sample was evaluated by a continuous flow reactor adapted from an existing design [37] as illustrated in Figure 2.5 (a). The volume of the cylindrical reactor, which was made of glass and covered with quartz glass window, was 141.3 mL (Φ60 mm × 50 mm) (Figure 2.5 (b)). One sample was placed in the middle of the reactor, and a 300 W xenon lamp with a light passed through a UV cut off filter (λ > 420 nm) was vertically placed outside the reactor as a light source. The required light intensity of 30 mW cm^{-2} on the surface of the samples was obtained by adjusting the distance between the lamp and the reactor. The initial concentration (1 ppm NO) of the testing gas was achieved with two mass

flow controllers supply. The relative humidity of the testing gas was control at 50 ± 2% by the gas-washing bottle before the gas entered the glass reaction chamber. The flow rate of the testing gas through the reactor was controlled at 1 L min^{-1} by a mass flow controller. Once the adsorption–desorption equilibrium reached, the lamp was turned on. The concentrations of NO and produced NO_2 were continuously measured using a NO_x analyzer (Model 42i, Thermo Environmental Instruments Inc). The removal amount of NO_x was calculated as following:

$$Q_{NO_x} = \left(\frac{f}{22.4}\right)\left\{\int([NO]_0 - [NO])dt - \int([NO_2] - [NO_2]_0)dt\right\}/(A \times T) \quad (2.1)$$

where Q_{NO_x} (μmol m^{-2} h^{-1}) is the amount of nitric oxides removed by the sample. $[NO]_0$ and $[NO_2]_0$ (ppm) are the initial concentration of nitrogen monoxide and nitrogen dioxide respectively without visible light. [NO] and $[NO_2]$ (ppm) are the outlet concentration of nitrogen monoxide and nitrogen dioxide respectively under visible light irradiation, t (min) is the time of removal operation and f (L min^{-1}) is the flow rate at the standard state (273K, 1.013 kPa). A (m^2) is the surface area of the sample. T (30 min) is the duration of the photocatalytic process.

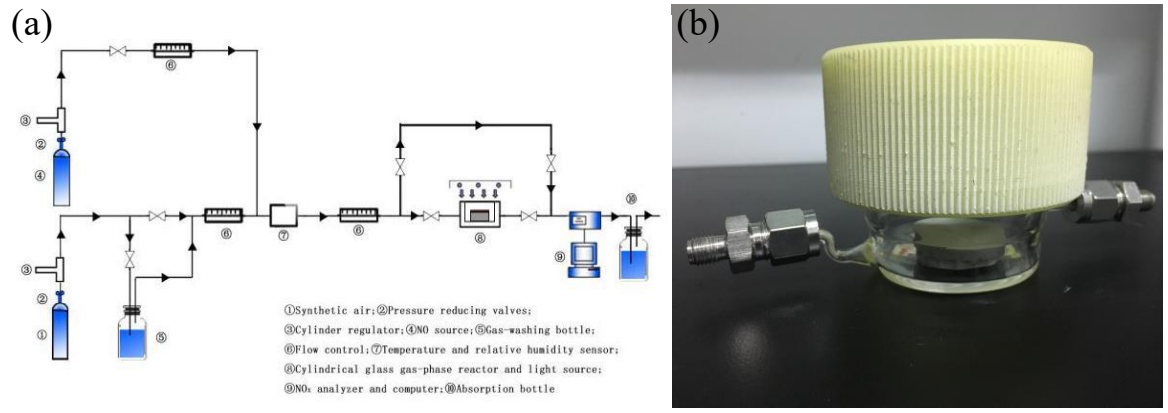

Figure 2.5 (a) Schematic diagram of the gaseous NOx removal experimental set-up; (b) Image of the reactor.

2.2.6.2. Self-cleaning test

The self-cleaning performance of the sample was evaluated following a procedure reported elsewhere [38]. Typically, a plastic ring (diameter 2.0 cm) was glued on the surface of as-prepared photocatalytic cementitious composites. 1 mL rhodamine B (RhB) solution with a concentration of 1.0 mmol L^{-1} was applied evenly on the surface of samples within the plastic ring. Then the specimens were oven dried at a temperature of 40 ℃ for 10 h. After drying, one sample was placed horizontally under a 300 W xenon lamp with a light passed through a UV cutoff filter ($\lambda > 420$ nm). The experiment obtained required light intensity of 30 mW cm^{-2} on the surface of the samples by adjusting the distance between the lamp and the samples. To avoid temperature rise, the samples were cooled down using an electrical fan during the operation. The color change of the dye applied on the photocatalytic specimens which were subjected to different light irradiation time (i.e., 0, 10, 20, 30, 40, 50 and 60 min) were pictured by a Nikon D7000 SLR camera (the distance between the camera lens and the specimen remained the same 10 cm). The software ImageJ64 analyzed the histogram analysis of the obtained images.

The removal efficiency of RhB was evaluated as follows:

$$\delta\% = \frac{C_0 - C_t}{C_0} \times 100\% \quad (2.2)$$

where C_0 and C_t are the concentration of the initial and remaining RhB respectively; t is the light illumination time.

2.3 Results and discussion

2.3.1. Effect of CNNs on early microscopic mechanical property of cementitious composites

The microscopic hardness of cementitious composites containing different dosages of CNNs (0, 0.5, 1, 2 % by weight of cement) that were cured for 7 days is displayed in Figure 2.6. With the addition of CNNs, a parabolic growth tendency of the microscopic hardness of

cementitious composites can be observed. The microscopic hardness of the cementitious composites with 2, 1 and 0.5% CNNs are 105.4, 115.3 and 117.9% respectively of the composite without CNNs due to the strengthening effect of CNNs. When the CNNs content is larger than 0.5%, the microscopic hardness tends to decrease slightly, attributed to the increased probability of agglomeration of CNNs in cementitious composites. This phenomenon agrees with a previous study that the cluster of the nano-materials weakened the microscopic hardness of cementitious composites [39]. Additionally, due to the high specific area, the addition of CNNs often leads to the increasing in the water demand, resulting in an increase in porosity [40]. This can also be responsible for the decline in microscopic hardness.

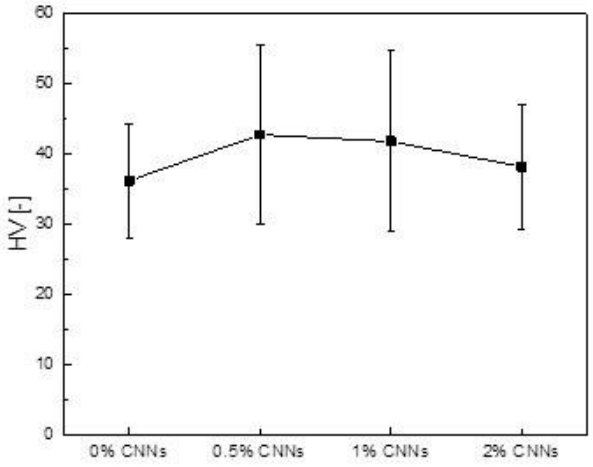

Figure 2.6 Microscopic hardness of cementitious composites with different content of CNNs.

2.3.2 Effect of CNNs on early hydration of cement

The hydration process of cementitious composites containing CNNs was monitored by isothermal calorimetry (TAM Air). Figure 2.7(a) shows the heat flow curves of the cementitious composites containing different dosages of CNNs. It is well known that cement hydration is a dissolution-precipitation process [41] and all specimens display two significant heat flow maxima during the main period. Figure 2.7(a) illustrates the first peak of the samples containing

CNNs starts earlier than that of the samples without CNNs. The addition of the CNNs greatly increases the intensity of the first heat peak, especially for the 2% addition. All the samples containing CNNs show a slightly higher intensity of the second heat evolution peak in comparison with the reference sample. Figure 2.7(b) shows the curves of the cumulative heat evolution during the first 100 h hydration. The increasing cumulative heat release at 2 h hydration can be observed with addition of CNNs, consistent with the heat evolution rate during the first heat peak. This indicates that the addition of CNNs can significantly accelerate the early hydration of cement, mainly resulting from the aluminate reaction [42]. The heat evolution of the second heat peak during the 2~100 h hydration can be attributed to the silicate reaction, C_3A dissolution and ettringite precipitation [43]. With the increasing time of hydration up to 100 h, although there is no significant difference of the cumulative heat, the samples containing 0.5 and 1% CNNs show a slight increase in the cumulative heat evolution with respect to that of pure cementitious composites, indicating an enhanced degree of hydration due to a multiplication of heterogeneous nucleation sites provided by CNNs. It is also widely accepted that the ultra-fine particles could act as potential heterogeneous nucleation sites for the hydration products, resulting in an acceleration of cement hydration [44, 45]. However, too much CNNs would obstruct the contact between cement particles and water, which is a disadvantage for the hydration process of cement. This results in a lower cumulative heat evolution at 100 h hydration for the 2% CNNs-added cementitious composites.

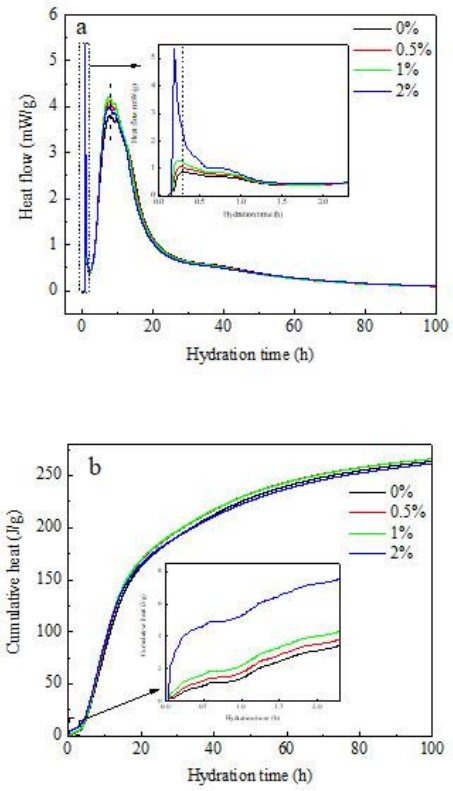

Figure 2.7 (a) Heat flow curves and (b) Cumulative hydration heat for cementitious composites with different content of CNNs.

In order to investigate the effect of CNNs on the hydration crystals of cementitious composites, XRD patterns of CNNs-added cementitious composites hydrated for 7 days were investigated. As shown in Figure 2.8 (a), although the characteristic peaks of the CNNs were not found in the XRD patterns due to its tiny amounts in the composites or its inherent low crystallinity, the peaks of calcium hydroxide (CH) and calcite were detected clearly for all samples while no other new phases were observed with increasing CNNs dosage. On the other hand, differences were found in the relative intensities of the (0 0 1) and (1 0 1) peaks of CH for all the samples, indicating the different preferential orientation growth of CH under conditions with different CNNs dosages. It can be observed in Figure 2.8 (b) that the relative intensities of

the (0 0 1) and (1 0 1) peaks decrease gradually with increasing CNNs dosage, suggesting that the CNNs lowered the orientation index of CH crystals, which can be attributed to the nucleation effect of CNNs. And the diminished orientation of CH crystals has been reported to be able to improve the interface structure of cementitious composites [46-47].

Figure 2.9 represents FTIR patterns of cementitious composites with different contents of CNNs hydrated for 7 days. After the introduction of the increased content of CNNs, the growing peak at 1250 cm^{-1} originated from tri-s-triazine heterocyclic rings in CNNs is observed clearly, suggesting that the composite materials were successfully prepared. The band appeared at 1650 cm^{-1} is attributed to the stretching and bending vibration of the chemically bound water in the calcium silicate hydrate (C-S-H) [48, 49]. A slightly negative shift of the peak at 1650 cm^{-1} with the addition of CNNs was observed indicating the formation of strong bond between C-S-H and CNNs. The interaction between the CNNs and the cement hydrates can improve the load-transfer efficiency from the cementitious composites to CNNs. Consequently, the microscopic hardness of the cementitious composite was enhanced. The peak at 3640 cm^{-1} is attributed to the O-H of portlandite phase [50]. For the 0.5 and 1% CNNs-added cementitious composites, the intensity of the O-H group of CH increase slightly compared to that of pure cementitious composite while the 2% CNNs-added cement composite shows a declined intensity. This suggests that the addition of 0.5 and 1% of CNNs helps increase the content of CH in cementitious composites while the addition of 2% CNNs exerts a negative impact on the formation of portlandite.

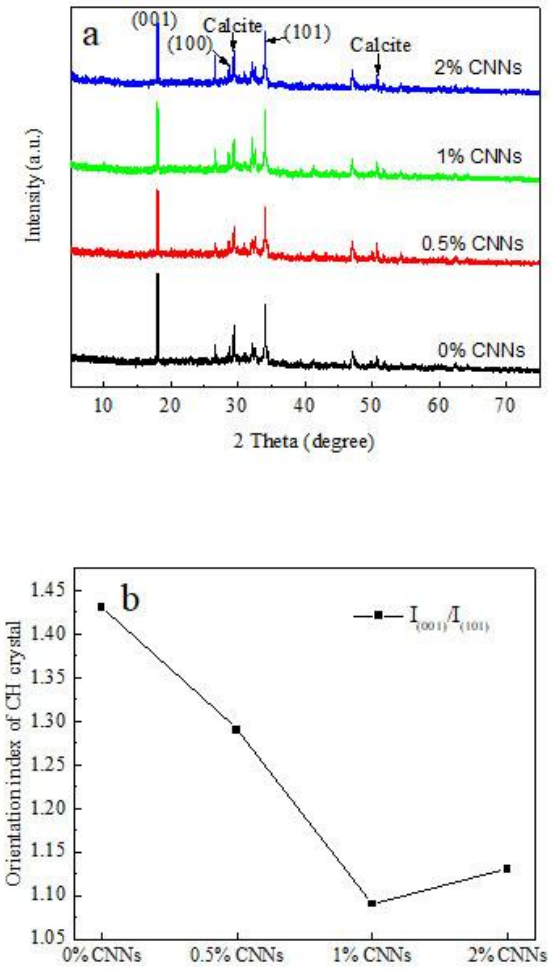

Figure 2.8 (a) XRD patterns and (b) orientation index of CH crystal of cementitious composites with different content of CNNs.

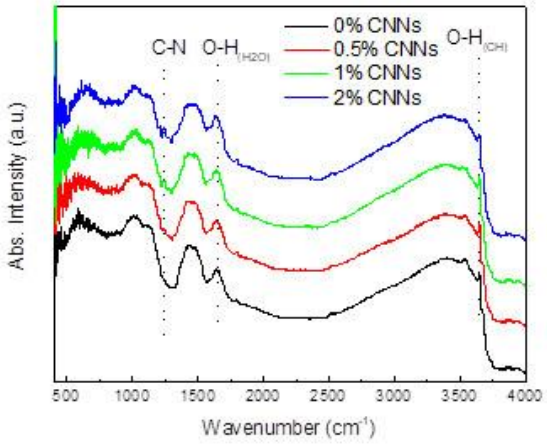

Figure 2.9 FTIR spectroscopy of cementitious composites with different content of CNNs.

Figure 2.10 shows the TG/DTG curve of cementitious composites with different CNNs dosages hydrated for 7 days. There are 3 endothermic peaks in the DTA curves attributed to the decomposition of C-S-H [51], CH [52] and calcite [53] respectively, which is in good agreement with the mineralogical characterization in XRD analysis (Figure 2.8 (a)). The content of non-evaporable water (NEW) is measured as the weight loss of the sample between 105 ℃ and 1000 ℃ [46]. Using formula (2.3), the NEW at different CNNs contents was calculated and shown in Figure 2.11.

$$NEW = W_{105℃} - W_{1000℃} - W_{CaCO_3} - W_{CNNs} \quad (2.3)$$

where NEW is the weight percentage of non-evaporable water; $W_{105℃}$ is the percentage of weight loss after 105 ℃ heat treatment; $W_{1000℃}$ is the percentage of weight loss after 1000 ℃ heat treatment; W_{CaCO3} and W_{CNNs} are the percentage weight loss of sample after the decomposition of $CaCO_3$ and CNNs, respectively.

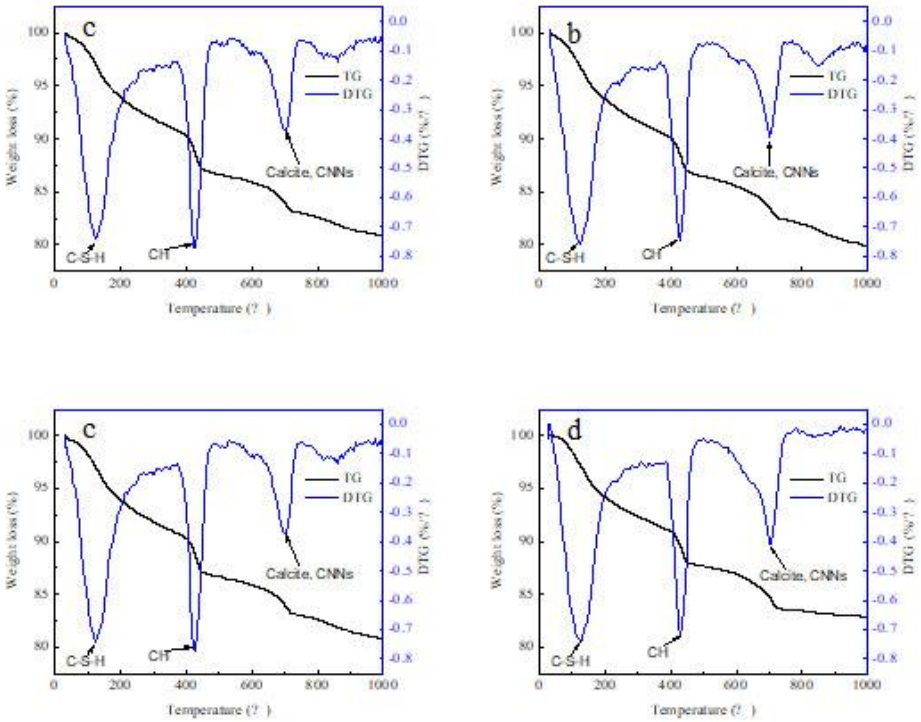

Figure 2.10 TG/DTG curve of the cementitious composites with different content of CNNs: (a) 0%, (b) 0.5%, (c) 1% and (d) 2% CNNs.

Figure 2.11 shows that the addition of 0.5 and 1% CNNs increases the NEW of cementitious composites. Especially, the NEW of 0.5% CNNs-added cement composite is 10.8% higher than that of cementitious composites without CNNs. With further increase of the CNNs dosage (2%), the NEW of cementitious composites decreases significantly. It can be deduced that a moderate amount of CNNs increases the degree of cement hydration due to the nucleation effect of CNNs, while too much CNNs impedes the polymerization of silicate chain resulting in a decreased hydration degree. The results from above hydration heat also support this observation. The weight loss between 400 ℃ and 500 ℃ is considered to be the decomposition of CH [54]. Figure 2.11 shows that with the addition of CNNs, a parabolic growth tendency of the content of CH can be observed. The content of CH in 0.5 and 1% CNNs-added cementitious composites is larger than that in other cementitious composites. This indicates that a moderate amount of

CNNs can facilitates the generation of CH in cementitious composites, which is in good agreement with the deduction from the FTIR analysis.

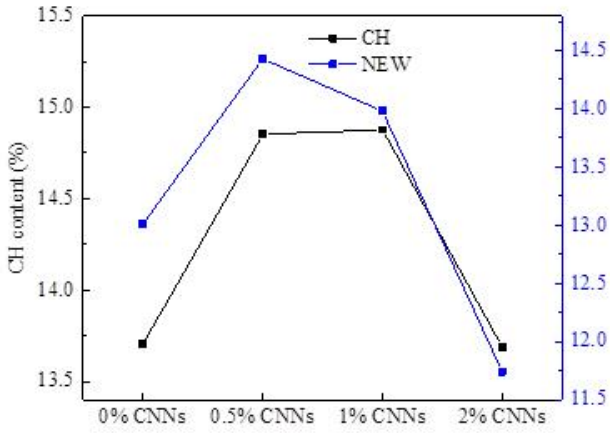

Figure 2.11 CH and NEW content of cementitious composites with different content of CNNs.

To further explore the effects of CNNs on cement hydration, the morphology of hydration products in the cementitious composites with different CNNs dosages hydrated for 7 days was investigated by the FESEM technique. Figure 2.12 shows the FESEM images of the microstructure of cementitious composites with CNNs. Noticeable changes were observed in terms of micro-morphology of the composite with the increase of CNNs dosage. For the plain cement composite, many immature cluster hydration products emerge in fracture surface, and some morphological needle-like hydration products disorderly stack with loose and porous structure (Figure 2.12 (a)). For 0.5% and 1% addition of CNNs (Figure 2.12 (b) and (c)), the characteristic immature cluster and needle-like hydrates are scarcely seen while the mature and compacted hydration products are uniformly distributed in the fracture surface, indicating higher hydration degrees compared to the plain cement paste. Those are consistent with the hydration degrees of CNNs-added cementitious composites inferred from the NEW. Most of CNNs embedded in the cementitious composites cannot be observed clearly due to the envelopment of

dense hydration products. Moreover, the presence of CNNs may provide good mechanical interlocking between hydration products, which contributes to the increased hardness of the cementitious composites. These results also confirmed the conclusion aforesaid that intermixing with CNNs helps improve the microscopic hardness of the cementitious composites. However, compared to the 1% CNNs-added sample, the microstructure of 2% CNNs-added cementitious composites presents more pores (Figure 2.12 (d)), which is attributed to that the excessive CNNs would reduce the cement hydration degree and increase the probability of bleeding. This can also be responsible for the decline in microscopic hardness.

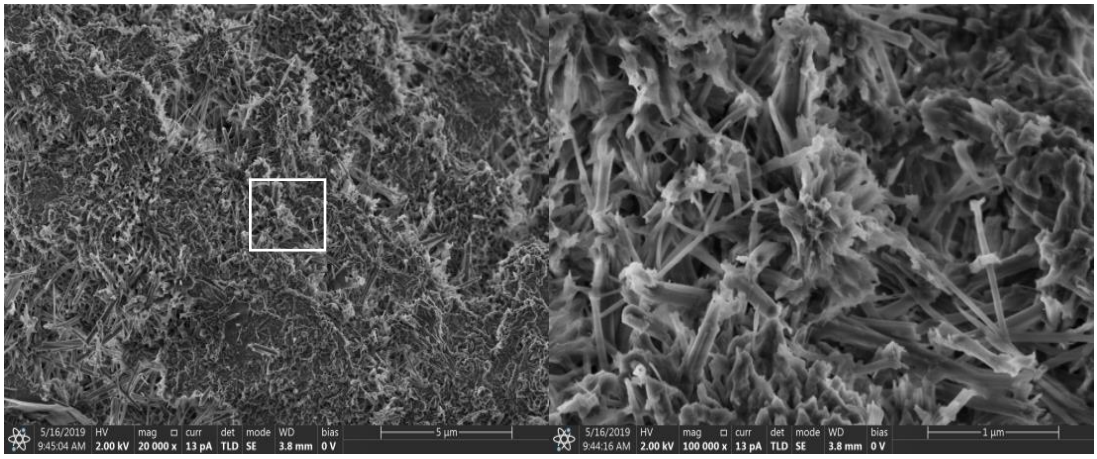

(a) 0% CNNs

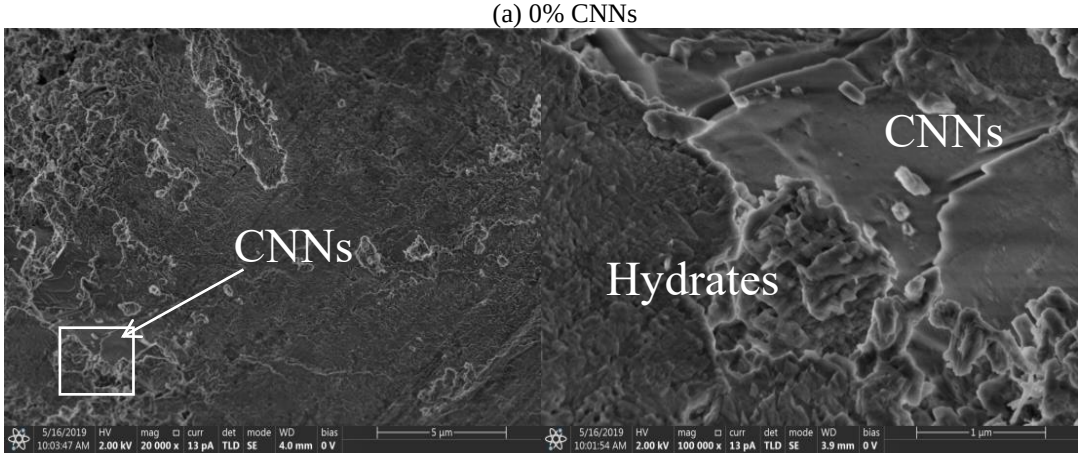

(b) 0.5% CNNs

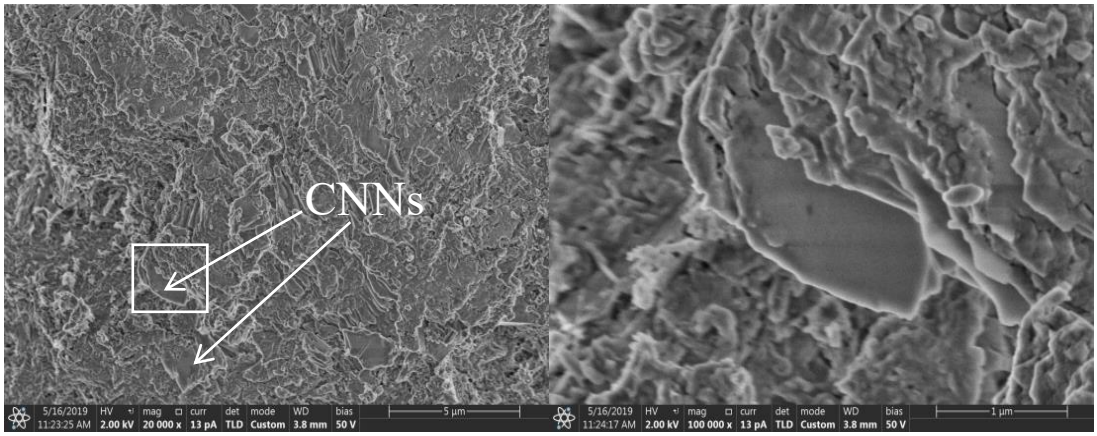

(c) 1% CNNs

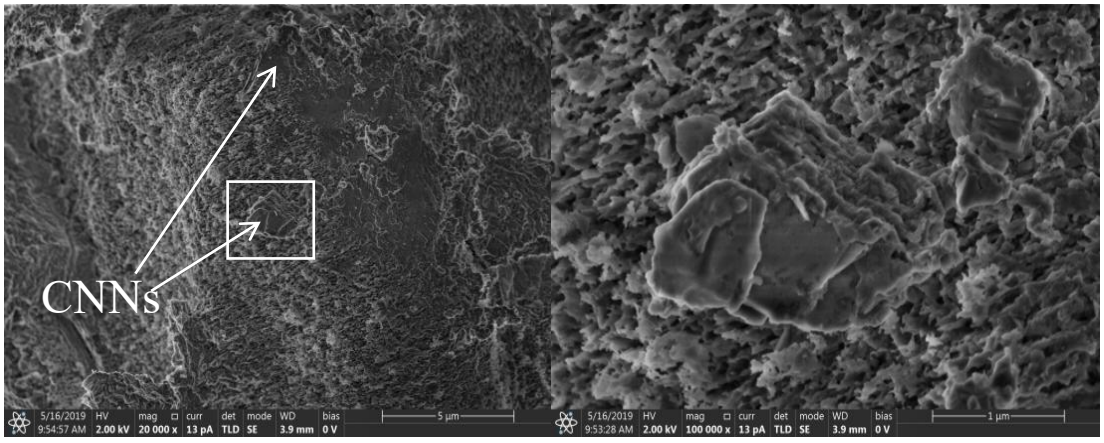

(d) 2% CNNs

Figure 2.12a-d FESEM images of the microstructure of the cementitious composites with different content of CNNs.

2.3.3. Visible light photocatalytic performance of the cementitious composites with CNNs

2.3.3.1. Visible light photocatalytic removal of NO_x

Cementitious composites intermixed with CNNs were employed for photocatalytic removal of NO_x in air under visible-light irradiation in a continuous mode to demonstrate their potential capability for air purification. Figure 2.13 shows the photocatalytic NO_x removal performances of cementitious composites prepared with CNNs as well as 2% TiO_2 under visible-light irradiation. As can be seen, the presence of CNNs significantly enhanced the photocatalytic performance of cementitious composites. Compared to TiO_2, CNNs have a narrower band gap

that can be excited directly by visible light. The removal of NO_x can be attributed to the reaction between NO_x and photogenerated radicals, producing a final product of NO_3^- [55, 56]. Only an increase of 51.6% in NO_x removal efficiency was observed for the samples with 1% CNNs, compared to the samples with 0.5% CNNs (83.5 μmol m^{-2} h^{-1}). This is because most of CNNs are enveloped by the denser hydration products in the 0.5 and 1% CNNs-added cementitious composites (Figures 2.12 (b) and (c)), and thus they are inaccessible to the reactants or the irradiation. However, the samples with 2% CNNs acquire a NO_x removal efficiency of 227.3 μmol m^{-2} h^{-1}, which is 1.8 times higher than that of samples with 1% (126.6 μmol m^{-2} h^{-1}). This larger increase in NO_x removal efficiency is attributed to not only the higher probability of CNNs in the surface of cementitious composites, but also the more porous structure for gas diffusion and light transmittance, which is consistent with the porous morphology observed in the FESEM images (Figure 2.12 (d)).

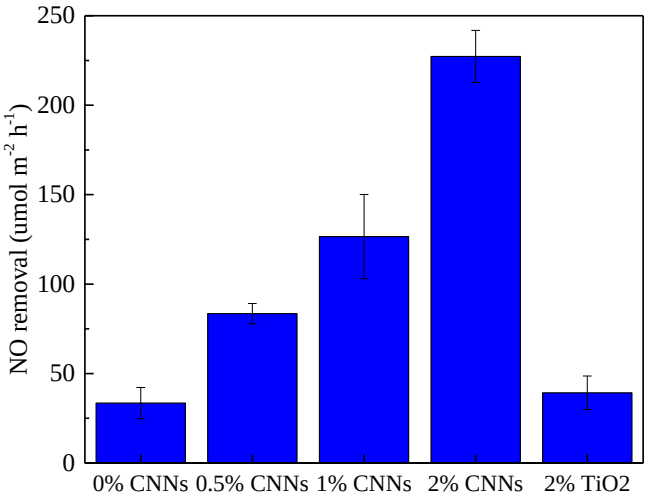

Figure 2.13 The visible-light photocatalytic NO_x removal of cementitious composites with CNNs and TiO_2.

2.3.3.2. Self-cleaning performance

Figure 2.14 presents the removal efficiency of rhodamine B (RhB) applied to the CNNs-added cementitious composites as well as to the one containing 2% TiO_2 under visible light irradiation. The discoloration function of the CNNs in the cementitious composites under visible light irradiation was observed clearly. Comparison of the pictures (Figure 2.15) taken before and after the irradiation experiments illustrates the self-cleaning effect more explicitly. Approximately 92% of color fading occurs after 40 min exposure for 2% CNNs sample while 40% of RhB bleach for the 2% TiO_2-added cement composite in the same period. The results indicate that compared with the TiO_2-added cementitious composites, the CNNs-added ones give a much better self-cleaning performance under visible light irradiation. However, the discoloration rate of the 0.5% CNNs sample was much lower than that of the 2% CNNs sample. It seemed that only part of the dyes near to the active sites of CNNs could be completely discolored leading to a much slower discoloration ratio. This is consistent with the finding shown in Figure 2.12(b) that compacted hydration products in the cementitious composites envelop many CNNs. With an increasing percentage of CNNs, the more porous structure (Figure 2.12(d)) can promote the percolation of the dye, resulting in a higher probability of contact of dye with CNNs. This could also contribute to the discoloration. It was also found that the color of the RhB applied on the control sample (without CNNs) faded to a certain extent, which was probably due to the direct photolysis or thermolysis of the dye [57].

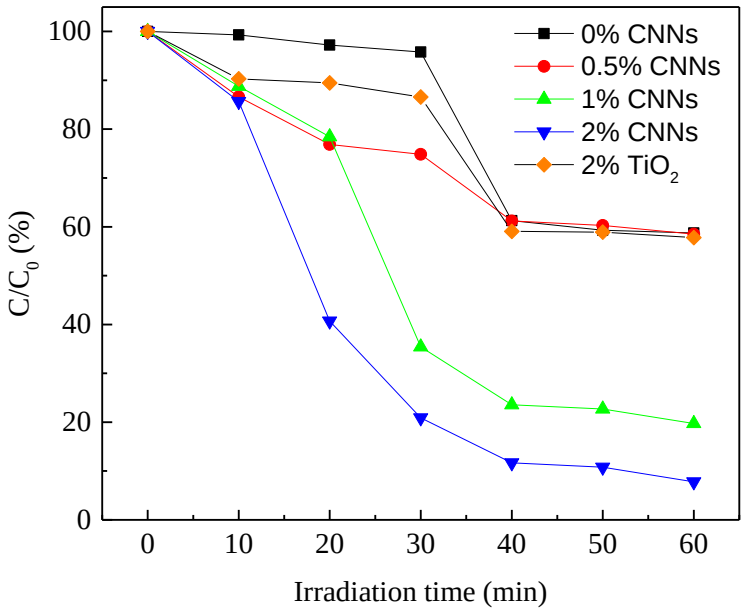

Figure 2.14 The removal efficiency of RhB applied on the cementitious composites with CNNs and TiO_2 under the irradiation of visible light.

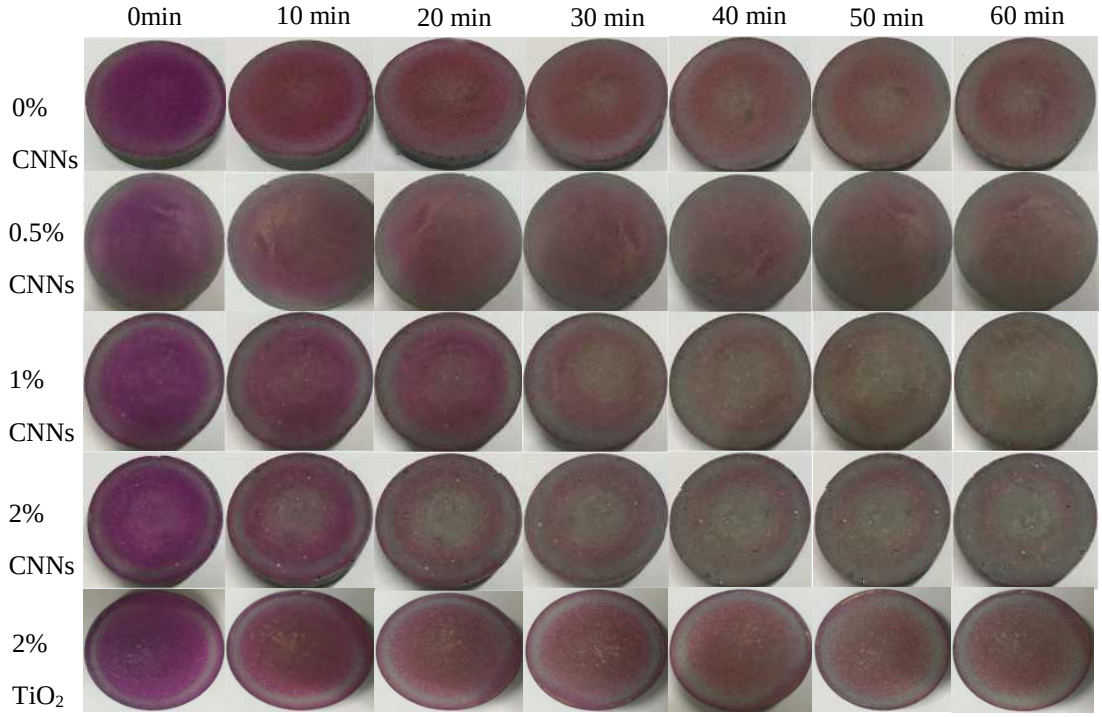

Figure 2.15 Color variation of RhB coated on cementitious composites with CNNs and TiO_2.

According to the foregoing results, compared with the one containing TiO_2, the photocatalytic cementitious composites incorporated with CNNs exhibited a much better visible light photocatalytic activity due to the suitable band gap. With the increase of CNNs content, the photocatalytic NO_x abatement and self-cleaning performance of the photocatalytic cement composite increased. For the 2% CNNs-added cementitious composites, excessive CNNs decreased the degree of cement hydration, but the microscopic hardness was 5.4% higher than that of the control due to the strengthen effect of CNNs. Moreover, among all the samples, the one with 2% CNNs showed the highest photocatalytic NO_x abatement efficiency of 227.3 μmol m^{-2} h^{-1}, and degraded the RhB within 40 min.

2.4 Conclusions

The main conclusions of this chapter are listed below.

1) With the increase of CNNs content, the hydration degree and micro-hardness increase first and then decrease. The microscopic hardness of 0.5% CNNs-added cement composite shows an improvement of 18% compared with the one without CNNs. For the 2% CNNs-added cement composite, excessive CNNs decreases the degree of cement hydration, but the microscopic hardness is still 5.4% higher than that of the control due to the strengthen effect of CNNs.

2) As the growth points for hydration products, the CNNs gave a strong bond with hydration products, which improved the load-transfer efficiency from the cementitious composites to CNNs.

3) With the increase of CNNs content, the photocatalytic NO_x abatement and self-cleaning performance of the photocatalytic cementitious composites increased. Among all the cementitious composites that were tested, the one with 2% CNNs showed the highest photocatalytic NO_x abatement efficiency of 227.3 $\mu mol\ m^{-2}\ h^{-1}$, and degraded the rhodamine B within 40 min. Compared with the TiO_2 based cementitious composites, the sample incorporated with CNNs gave a much better visible light photocatalytic activity due to the suitable band gap. It was found that a moderate amount of CNNs (below 2%) could be used in cementitious composites for the photocatalytic depollution performance without adverse effect on mechanical properties of the cementitious composites. This work is expected to help broaden the application of photocatalytic cementitious materials in sustainable building and constructions for improved environmental pollution mitigation.

CHANPTER 3 WASHING RESISTANCE OF PHOTOCATALYTIC CEMENTITIOUS MATERIALS BASED ON G-C_3N_4 NANOSHEETS-RECYCLED ASPHALT PAVEMENT AGGREGATE COMPOSITES

3.1 Introduction

The oxide of nitrogen (commonly expressed as NO_x, mainly NO and NO_2), primarily from vehicle emissions, is the major source to the acid rain and urban smog. Application of photocatalysis in cementitious materials has gained considerable attention for facilitating the oxidative decomposition of NO_x [58-61]. The photocatalytic building materials based on titanium dioxide (TiO_2), as benchmark products, have been reported [62-64]. In spite of its favorable air purification capability as a photocatalyst, TiO_2 suffers from such drawbacks as low exploitation of sunlight (due to wide band gap above the range 3.0-3.2 eV) and high recombination rate of photo-generated electrons and holes [65, 66]. In particular, TiO_2 has recently been determined a possible carcinogen when inhaled [67, 68]. These are significant obstacles impeding a broad application of TiO_2 in building materials. The development of a nontoxic photocatalyst with outstanding visible light activity to be used in building materials is highly and urgently needed.

Graphitic carbon nitride nanosheets (CNNs), a typical two-dimensional layered material, are well known as a nontoxic metal-free semiconductor. CNNs are notable for unique features such as high thermal and chemical stability, fast separation of photo-excited carriers and suitable band gap (2.7 eV). As such, CNNs have been considered as a prospective photocatalyst for many applications including water splitting [69], CO_2 reduction [70] and pollutants abatement [71, 72] under visible light irradiation, and can be an excellent alternative to TiO_2.

Today, most photocatalytic building materials are prepared by coating or mixing photocatalyst with cementitious materials. Photocatalyst-intermixed building materials with air purification [73, 74] and self-cleaning properties [75, 76] have been reported. It is worthwhile to note that most of the photocatalyst reported are in the internal structure of the products. The direct interaction of the photocatalyst with sunlight and pollutants remains limited. A higher tendency for agglomeration of the photocatalyst particles has been observed in cement-based systems [77], resulting in a low efficiency of the photocatalyst. Note that both flexural and compression strength are decreased for mortar specimens with a higher amount of TiO_2 [78]. Coating photocatalyst on the surface of building materials has been proven as an efficient way to improve the efficiency of photocatalytic activity in practical service conditions [79, 80]. The photocatalytic coatings readily peel off when suffering from traffic loading and natural weathering, therefore weakening the catalytic performance and shortening the service life. Studies regarding the influences of cement circumstance on the behavior of photocatalyst have proven that the high pH value, various ion species and the surface carbonization of gas-solid interface can adversely affect the photocatalytic performance, regardless of whether the photocatalysts were coated on the surface or mixed with the matrix [81, 82]. Attempts to improve the photocatalytic effects of the photocatalytic building materials include utilization of porous cement substrate [83], regulation of the substrate microstructure [84] and surface modification of the photocatalyst [85]. These strategies somewhat improved the photocatalytic efficiency and long-term performance of the photocatalytic cementitious composites due to less aggregation and higher exposure degree of photocatalyst particles in cement matrix. However, the intrinsic cement chemistry and the increasing production cost due to surface modification remain a significant barrier that restrict a large-scale application of the photocatalytic building materials.

The photocatalytic exposed aggregate cementitious materials (PEACM) have recently been proposed for the maintenance of building aesthetics and environmental remediation [86, 87]. This exposed photocatalytic aggregate can sufficiently detach the photocatalyst chemistry from the effects of cement chemistry [84, 88]. In order to obtain a desired resistance to weathering or abrading, some procedures that are inconvenient and costly such as high temperatures (400℃) [86], alkali activation [88, 89] and negative pressure [90] may be required to form a strong bond between aggregate and photocatalyst.

Recycled asphalt pavement aggregate (RAPA) consisting of crushed basalt rock and residual asphalt binder has been used to replace natural fine and coarse aggregates in cement composites [91, 92]. This has been considered effective to reduce the waste asphalt, more than 60 million tons in China annually produced, and substantially contribute to cost savings and conservation of natural aggregate sources [93, 94]. The residual asphalt on the surface of RAPA can restore the binder property after reheating [95, 96], and contribute to a good adhesion for supporting the photocatalyst. In this chapter, a photocatalytic recycled asphalt pavement aggregate (PRAPA), namely g-C_3N_4 nanosheets-recycled asphalt pavement aggregate composites, was prepared for the first time by immersion and evaporation. By making use of the binder property of the residual asphalt, a strong bond between CNNs and RAPA can be obtained. The photocatalytic exposed aggregate cementitious materials (PEACM) were prepared by loading the PRAPA on the surface of cement paste at its initial setting. For comparison, the photocatalytic standard sand (PSS) containing CNNs and standard sand were also prepared via the same method. Their respective photocatalytic NO_x removal efficiency and washing resistance (in short for the capability to resist rain-washing) were evaluated and compared. The washing resistance is an important index for evaluating the durability of photocatalytic materials. The

physical characteristics, such as the apparent appearance, CNNs amount, morphology and element content of the surface specimen, were investigated before and after rain-wash. The results will provide a new framework for preparation of highly cost-effective photocatalytic building materials, and facilitate a desirable option for recycling waste asphalts mixtures.

3.2 Experimental

3.2.1. Materials

The experiment used RAPA with approximately 2.6% residual asphalt by weight of aggregate. The China ISO standard sand (SS) from Xiamen ISO Standard Sand Co., Ltd was used as a control group. The physical characteristics and chemical composition of RAPA and SS are listed in Table 3.1 and Table 3.2, respectively. A grade of 42.5 ordinary Portland cement, as well as Melamine and ammonium chloride, was used. Deionized water was used throughout the experiments. Details for the synthesis of CNNs have been given in Subsection 2.2.2.

Table 3.1 Physical characteristics of RAPA and SS.

Sample	Fineness modulus	Specific gravity (g/cm^3)	Density (kg/m^3)	Water absorption (%)
RAPA	3.89	2.65	1439	0.98
SS	2.37	2.61	1642	1.15

Table 3.2 Chemical composition of RAPA and SS (%).

Sample	MgO	Al_2O_3	SiO_2	SO_3	K_2O	CaO	Fe_2O_3
RAPA	6.81	9.72	54.3	1.13	1.95	22.8	3.29
SS	0.04	1.52	92.68	0.04	0.48	3.83	1.41

3.2.2. Preparation of PRAPA

The PRAPA was prepared simply by immersion and evaporation. A diagram illustrating the preparation process of the PRAPA is shown in Figure 3.1. In brief, the CNNs suspension was obtained via sonication of the CNNs in absolute alcohol for 2 h with an ice bath. The different concentrations of the CNNs suspension were designed as 1 g L^{-1}, 3 g L^{-1}, 5 g L^{-1} and 7 g L^{-1}. Afterwards, the 30 g of RAPA was distributed uniformly and immersed into 100 ml of CNNs suspension for 10 h. Subsequently, the CNNs suspension was evaporated to enable CNNs to attach on RAPA at 105 ℃ for 12 h. The prepared photocatalytic RAPA was denoted as PRAPA-n, where n was the coating concentration of CNNs suspensions (n=1, 3, 5, 7). The PSS with CNNs concentration of 5 g L^{-1}, denoted as PSS-5, was prepared via the foregoing method as a reference sample.

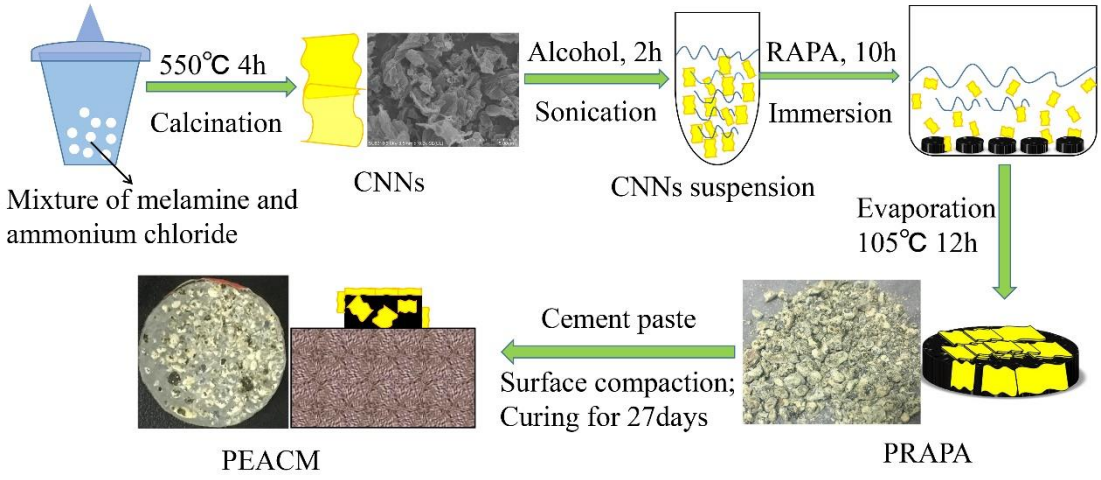

Figure 3.1 Schematic illustration of the preparation of PRAPA and PEACM.

3.2.3. Preparation of PEACM

The PEACM, with PRAPA embedded to the surface of cement paste, was prepared according to a previous work [87]. Figure 3.1 illustrates the preparation process of PEACM. In detail, the ordinary Portland cement and water (water/cement ratio=0.35) were mixed in a standard lab mixer for 2 min with a revolution speed of 300±5 r min^{-1}. The fresh cement paste

was cast into cylinder mold with the dimensions of Φ30 × 5 mm. Subsequently, 1.5 g of PRAPA was distributed on the top surface of the cement pastes and compacted for 1 min to ensure that the PRAPA was embedded onto the surface of the pastes. One day after the casting, the specimens were demolded and cured in a chamber at 20 ± 2 ℃ and over 95% relative humidity for another 27 days before subjecting to the preassigned tests. Finally, the PEACM specimens were successfully prepared and denoted as PRAPA-n-PEACM, where n was the coating concentration of the CNNs suspensions (n=1, 3, 5, 7). For comparison, the PEACM was also prepared with PSS-5 via the foregoing method, and denoted as PSS-5-PEACM.

3.2.4. Simulation of rain-wash actions

To investigate the resistance of PRAPA and PEACM to rain-wash in real service conditions, a simulation of the rain-wash was carried out and then applied for testing specimens. Figure 3.2 depicts a sketch of the experimental set-up for the simulated rain-wash. For the PRAPA, a previous protocol using the water immersion with sonication was adopted to simulate the rainwater immersion and heavy rainfall, and was also used to evaluate the durability of TiO_2-quartz composites [98]. As for the PEACM, the water spraying has been commonly adopted in experiments to simulate rainfall condition [99, 100] and it can also be used as an accelerated washing action [101]. In detail, the PRAPA specimens were immersed in deionized water with sonication for 20 min, using a Shu Mei ultrasonic bath (KQ-200KDB, 40 kHz, 200 W). After that, the specimens were washed with deionized water several times until a clear solution was observed, and then oven dried at 105 ℃ for 24 h before subject to further testing. For the PEACM, the specimen was inclined at 30° and the tap water was sprayed manually on the surface of the specimens at 600 ml min^{-1} (totally 6 L) with a distance of about 30 cm in a vertical direction. Afterwards, the specimen was oven dried at 105 ℃ for 24 h before they are ready for

further tests.

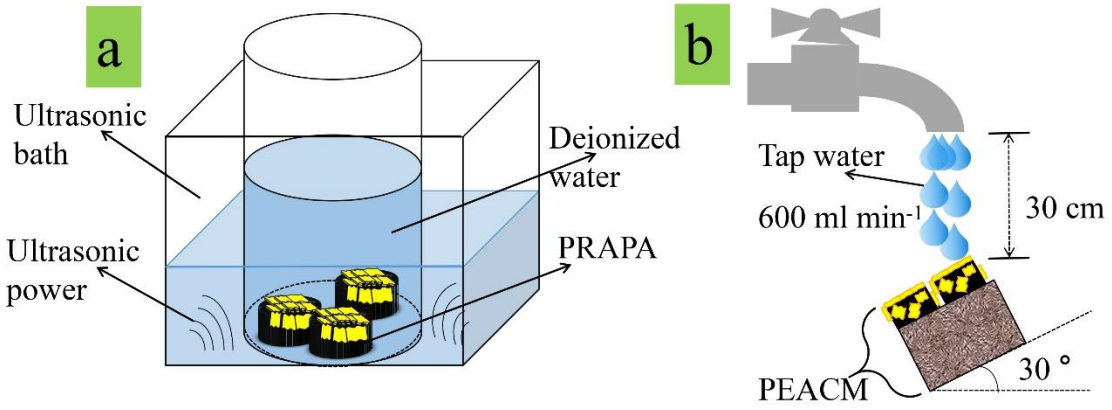

Figure 3.2 Sketch of the experimental setup for (a) PRAPA and (b) PEACM under rain-wash.

3.2.5. Characterization

The apparent appearance of the samples was observed by Nikon D7000 SLR camera with focal length of 30 mm. The amount of CNNs present on the sample surface was determined using an analytical balance (Sartorius BSA124S) with a precision accuracy of 0.1 mg. Typically, the mass of the non-coated sample was measured first and denoted as M_0. After the coating procedure, the mass of the coated sample was measured and denoted as M_1. The mass difference between M_0 and M_1 is regarded as the CNNs amount on the sample before washing. After washing, the mass of the coated sample was measured and denoted as M_2, and the mass difference between M_0 and M_2 is the CNNs amount on the sample after washing. The same sample was used when it was non-coated, coated and washed. For each test for CNNs amount, three replicate samples were used and the average value was used for report. Prior to mass measurements, samples were oven dried at 105℃ for at least 10 h to ensure complete water removal. Then the samples cooled down gradually in a desiccator container for 60 min. Scanning Electron Microscopy (SEM) equipped with Energy-dispersive X-ray spectroscopy (EDS) analysis (Bruker Quanta 250) examined morphology and elemental composition of the samples

before and after rain-wash.

3.2.6. Visible light photocatalytic activity experiments

The capability for air purification of the as-prepared PRAPA and the associated PEACM was evaluated by the removal efficiency of NO_x in a continuous reactor under visible light irradiation. The gaseous NO_x removal experimental set-up is shown Figure 2.5a. The cylindrical reactor, with a dimension of Φ60×50 mm, was made of glass and covered with quartz glass window (Figure 2.5b). A 300 W xenon lamp with a light passing through a UV cut off filter (λ>420 nm) was vertically placed outside the reactor as a light source. The required light intensity on the surface of the samples was 30 mW cm^{-2}, obtained by adjusting the distance between the lamp and the reactor. To avoid temperature rise, the reactor cooled down using an electrical fan during the operation. The NO gas was supplied from a compressed gas cylinder with 5 ppm NO concentration (N_2 balance), and the air provided by a compressed cylinder as well. The desired concentration (1000 ± 50 ppb NO) of the testing gas was achieved by mixing air stream and NO gas. The relative humidity (RH) of the testing gas was controlled at 50 ± 2% by passing the air streams through a water bubbler. The flow velocity of the testing gas was controlled at 0.6 L min^{-1} by mass flow controllers. Once the adsorption-desorption equilibrium was reached, the lamp was turned on, and the photocatalytic NO_x degradation test was proceeded for 30 min. The concentration of NO_x was continuously measured using a NO_x analyzer (Model 42i, Thermo Environmental Instruments Inc).

1.5 g of the as-prepared PRAPA was uniformly distributed in a cylindrical dish (diameter 30 mm), and the thickness of this PRAPA sample is approximately 2-3 mm. Subsequently, the cylindrical dish was put inside the reactor for the photocatalytic NO_x removal experiment. The PEACM was directly put in the middle of the reactor for the photocatalytic NO_x abatement test.

Each test used three replicates and the average value with the standard deviation adopted for report. The tests were carried out at ambient temperature (25 ± 2℃). The removal amount of NO_x was calculated according to the formula as follows [89]:

$$Q_{NO_x} = \left(\frac{f}{22.4}\right)\left\{\int([NO]_0 - [NO])dt - \int([NO_2] - [NO_2]_0)dt\right\}/(A \times T) \quad (1)$$

where Q_{NO_x} (μmol m^{-2} h^{-1}) is the amount of nitric oxides removed by the test sample. $[NO]_0$ and $[NO_2]_0$ (ppb) are the inlet concentration of nitrogen monoxide and nitrogen dioxide, respectively. [NO] and $[NO_2]$ (ppb) are the outlet concentration of nitrogen monoxide and nitrogen dioxide, respectively, t (min) is the time of removal operation and f ($L \cdot min^{-1}$) is the flow rate at the standard state (273K, 1.013 kPa). A (m^2) is the surface area of the PEACM or the cylindrical dish. T (30 min for all experiments) is the duration of the photocatalytic process and 22.4 represents that the volume of 1 mol ideal gas at the standard state is 22.4 L (ideal gas law).

3.3 Results and discussion

3.3.1 Characteristics of PRAPA and PSS

Figure 3.3 shows the surface appearance of RAPA, SS and PRAPA-5 as well as PSS-5 before and after rain wash simulated according to the set-up provided in Figure 3.2. The SS is partially light-yellow colored after coated with CNNs. This is consistent with the color of CNNs [102]. Compared with the original color of RAPA, obvious light-yellow coating layer on the surface of PRAPA-5 can be observed, suggesting a complete coverage of CNNs on the surface of RAPA. For the PSS-5, the light-yellow color almost disappears when it was subjected to the rain wash, pointing to a significant loss of CNNs on the surface of SS. Surprisingly, as for PRAPA-5, no significant difference is observed before and after washing, indicating a strong resistance to exfoliation of CNNs from the substrate.

Figure 3.3 Apparent appearance of (a) SS, (b) PSS-5 before washing, (c) PSS-5 after washing, (d) PSS-5 after water dropping, (e) RAPA, (f) PRAPA-5 before washing, (g) PRAPA-5 after washing and (f) PRAPA-5 after water dropping.

Interestingly, compared with the phenomena of hydrophilicity in PSS-5, the macroscopic hydrophobicity can be found on the surface of PRAPA-5 (Figure 3.3). The hydrophobicity of asphalt and g-C_3N_4 can account for the visible hydrophobicity on the PRAPA-5 [103, 104], while the hydrophilicity of sand is responsible for the wettability of PSS-5 [105]. The characteristic of the obvious hydrophobicity in PRAPA can effectively promote the water drop rolling from its surface and decrease significantly the contact area between water and PRAPA when subjected to rain-wash conditions. Consequently, the adhesion between water and PRAPA is quite limited compared to PSS. This may be responsible for the strong washing resistance to exfoliation of CNNs from the PRAPA.

The amount of CNNs attached on the PRAPA and PSS before and after washing is shown in Figure 3.4. With a higher concentration of CNNs, the CNNs amount on the PRAPA increases continuously, but that such increase tends to be slow. For the PRAPA-1, the CNNs amount is approximately 3.3 mg and increases up to about 7.5 mg at 3 g L^{-1} CNNs concentration. The CNNs amount is approximately 9.3 mg and 10.4 mg for PRAPA-5 and PRAPA-7, respectively.

The slight increase of the CNNs amount is attributed to the limited surface area of the RAPA. The excessive CNNs tend to agglomerate rather than attach on the surface of RAPA when the available surface of RAPA has been almost coated with CNNs. Additionally, a lower amount of CNNs (7.2 mg) is observed in the PSS-5 than in the PRAPA-5, indicating a larger loading of CNNs in RAPA than in SS.

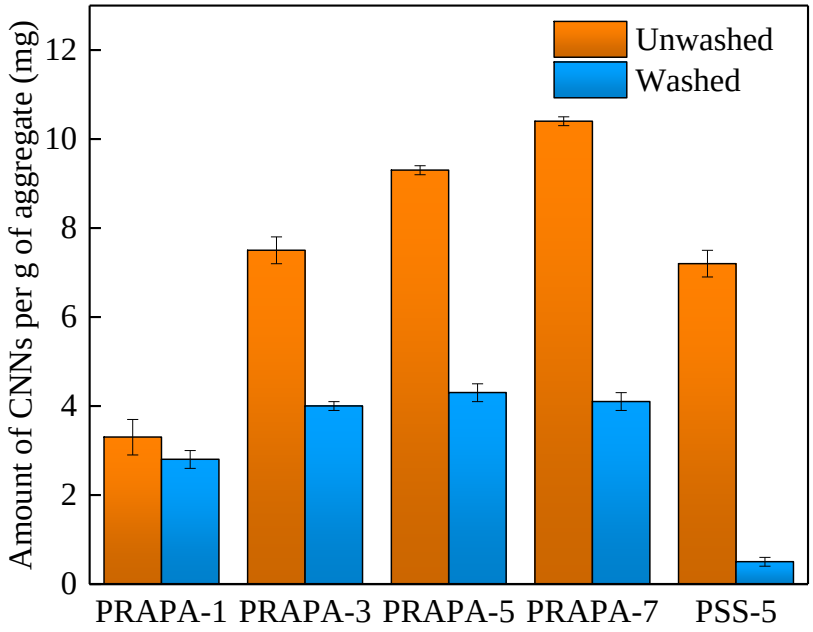

Figure 3.4 Amount of CNNs attached on PSS-5 and PRAPA with different concentrations of CNNs suspensions before and after rain-wash.

To test the adhesion of CNNs to substrates, the as-prepared PRAPA and PSS-5 were subjected to the rain-wash. As shown in Figure 3.4, a considerable amount of CNNs of approximately 4.0 mg, which is 8 times larger than that of PSS-5, is present in PRAPA-3, PRAPA-5 and PRAPA-7. This suggests that the amount of CNNs attached firmly on the PRAPA is approximately 4.0 mg CNNs per g PRAPA at most. Table 3.3 shows the loss rate of CNNs on

the surface of PSS-5 and PRAPA with different concentrations of CNNs after the rain-wash. A massive loss of CNNs, about 93.1%, is observed on the PSS-5, indicating a weak adhesion of SS. The loss rate of CNNs in PRAPA, although increasing up to 60.6% with increasing concentration of CNNs, is remarkably lower than that of PSS-5. It demonstrates that compared with the PSS, the PRAPA displays a better resistance to rain-wash, a finding in good agreement with the apparent appearances as described earlier (Figure 3.3).

Table 3.3 Loss rate of CNNs on the surface of PSS-5 and PRAPA with different concentrations of CNNs suspensions after rain-wash (%).

	PRAPA-1	PRAPA-3	PRAPA-5	PRAPA-7	PSS-5
Loss rate	15.2	46.7	53.7	60.6	93.1

The surface morphologies and elemental analyses of SS and RAPA are shown in Figure 3.5. The SS shows a smooth surface without obvious cracks and pores, accounting for the weak adhesion between photocatalyst and SS [89]. A rough surface appearance on the RAPA can be attributed to the residual asphalt layer. It is reasonable to consider that the cohesive property of the residual asphalt results in a good adhesion to support the CNNs. Figure 3.6 shows that the compactness and thickness of the CNNs coatings increase with a higher concentration of CNNs. The surfaces of PRAPA-5 and PRAPA-7 are enveloped by CNNs completely. Nevertheless, the thin and fragmented CNNs coating is observed on the surface of PSS-5, in other words, the massive glossy surface region of SS is exposed. This confirms that the smooth surface of SS is undesirable to the attachment of CNNs.

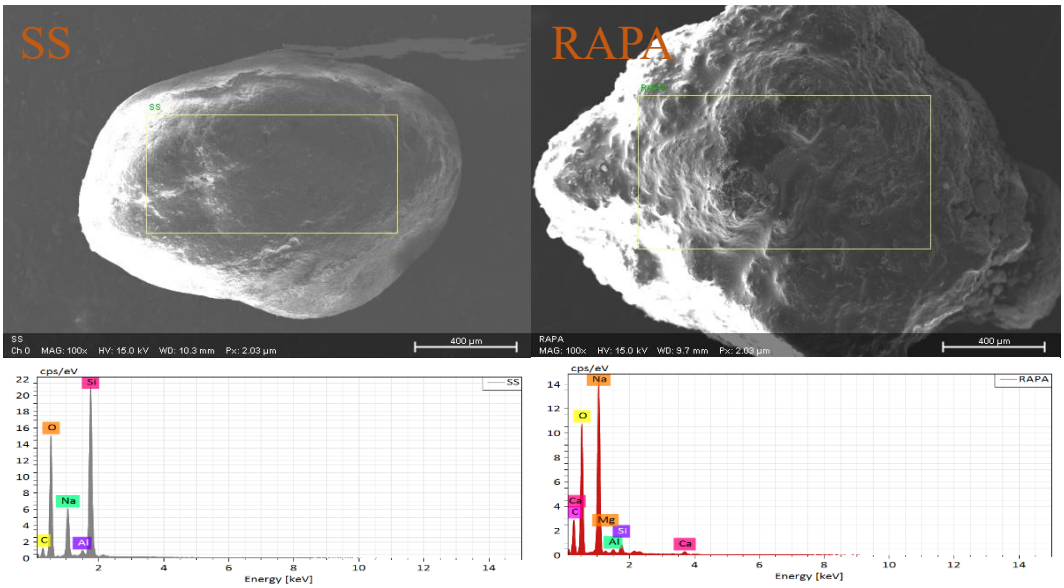

Figure 3.5 SEM morphologies and EDS elements characteristics of SS and RAPA.

The CNNs content on the surface of PRAPA and PSS can be measured by SEM-EDS analysis. The N signal is regarded coming from the CNNs attached on the surface of the aggregate (RAPA and SS). As indicated in Table 3.4, the N content of all PRAPA increases obviously compared to that of RAPA. The N content on the surface of PRAPA-3 is approximately 25.8% and increases to approximately 30.2% for PRAPA-5. Of interest to note is that the N content remains nearly constant with a further increase of CNNs concentration to 7 g L^{-1} (PRAPA-7). It is worth mentioning that the N signal at the bottom of CNNs coatings may not be trapped when the thickness of coatings exceeds 3.7 µm according to the configuration of this instrument. This demonstrates that with increasing concentration of CNNs from 5 g L^{-1} to 7 g L^{-1}, the incremental amount of CNNs contributes to the improvement of coating thickness via the overlapped CNNs, while the surface area of CNNs coatings remains unchanged, which coincides with the SEM morphologies (Figure 3.6). The N content on the surface of PSS-5 (22.7%) is significantly lower than that of PRAPA-5 (30.2%), which is in good agreement with the amount of CNNs (Figure 3.4).

Table 3.4 N content on the surface of SS, RAPA, PSS-5 and PRAPA with different concentrations of CNNs suspensions before and after rain-wash (%).

	SS	RAPA	PRAPA-1	PRAPA-3	PRAPA-5	PRAPA-7	PSS-5
Before	0	0	17.2±7.6	25.8±9.3	30.2±12.4	30.7±13.2	22.7±9.3
After	-	-	13.6±5.8	19.8±7.5	21.2±9.0	21.8±9.2	3.3±2.1

After the rain-wash, some thin and fragmentary CNNs coatings remain on the surface of PRAPA (Figure 3.7). Compared with the CNNs attached directly on residual asphalt, both the overlapped CNNs and the CNNs adsorbed on the surface without asphalt can be removed easily after exposure to the rain-wash. Whereas, little CNNs and N content (3.3%) can be observed in PSS-5 (Figure 3.7), indicating a weak washing resistance of PSS. It is worth noting that the considerable content of N can be observed in PRAPA-1 (13.6%), PRAPA-3 (19.8%), PRAPA-5 (21.2%) and PRAPA-7 (21.8%) after exposure to the rain-wash. This is in good agreement with the CNNs amount after subject to the rain-wash (Figure 3.4) and provides further evidence for the strong resistance of the PRAPA to rain wash as compared with the PSS.

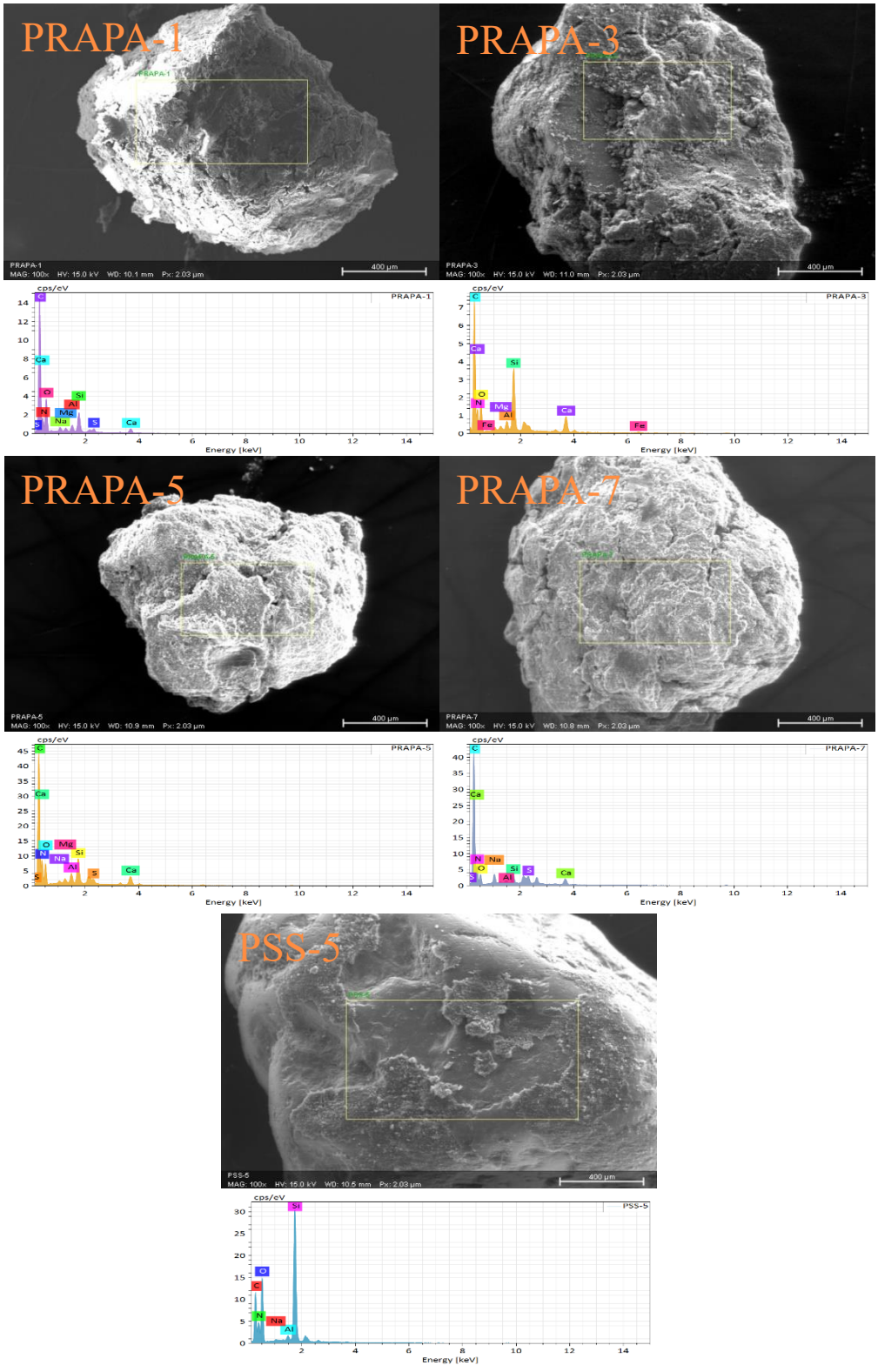

Figure 3.6 SEM morphologies and EDS elements of PSS-5 and PRAPA with different concentrations of CNNs suspensions.

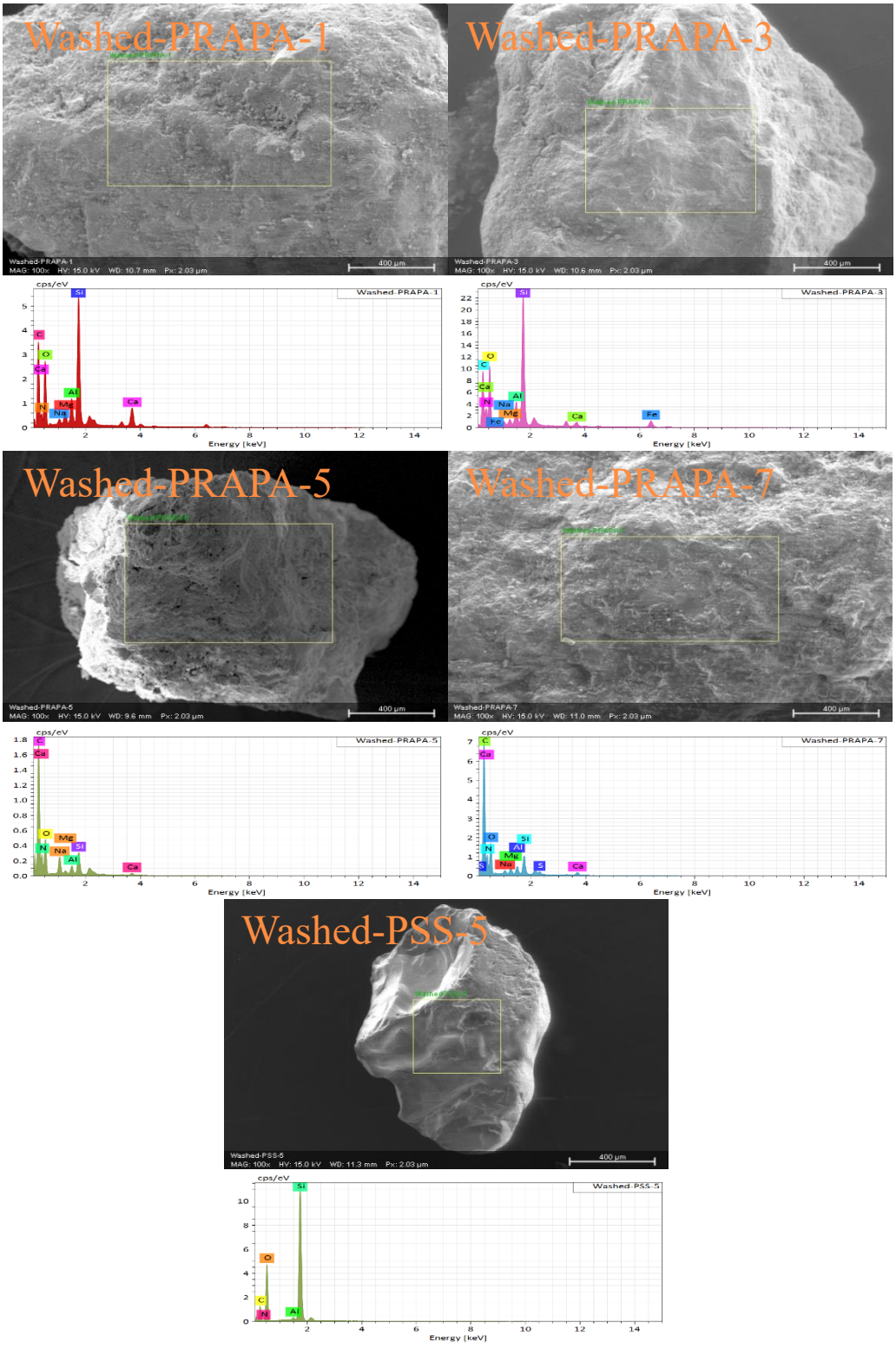

Figure 3.7 SEM morphologies and EDS elements of PSS-5 and PRAPA with different concentrations of CNNs suspensions after rain wash.

The above findings indicate that the CNNs were randomly distributed on the surface of

RAPA with or without residual asphalt. With the further increase of CNNs concentration, overlap of the CNNs occurs due to their high surface energy. When subjected to rain-wash, most of the CNNs are attached directly on the surface of asphalt due to the good adhesion of residual asphalt, while both the overlapped CNNs and the CNNs adsorbed on the surface without asphalt are removed easily. This suggests that the adhesion of the aggregate substrate is an important factor affecting the durability of the CNNs-aggregate composites in real service condition. Using RAPA as a substrate for the CNNs is desirable to virgin aggregates in terms of the enhancing bond between CNNs and aggregate. It can be expected that the RAPA with a greater amount of residual asphalt have higher surface area coated with residual asphalt, which are able to firmly attach more CNNs particles. Considering the high hydrophobicity and good adhesion of residual asphalt [106], it is difficult for water to replace the CNNs on the surface of PRAPA under heavy rainfall conditions. Consequently, most of the CNNs remain attached directly on the surface of PRAPA. In contrast, it is easy for water to occupy the surface of SS due to its natural hydrophilicity [105]. Therefore, the CNNs on the surface of the SS can be easily replaced by water due to the weak adhesion between CNNs and smooth surface of SS. This explanation also applies to the observed phenomenon in this chapter.

3.3.2. Photocatalytic performance

Figure 3.8 shows the photocatalytic NO_x removal performance of PRAPA and PSS before and after exposure to the rain-wash. All PRAPA display effective NO_x removal under visible light irradiation. Before exposure to the rain wash, as the CNNs concentration increases from 0 g L^{-1} (as reference) to 5 g L^{-1}, the photocatalytic NO_x removal efficiency of PRAPA increases clearly, with the highest photocatalytic efficiency of 507.4 μmol m^{-2} h^{-1} in PRAPA-5.

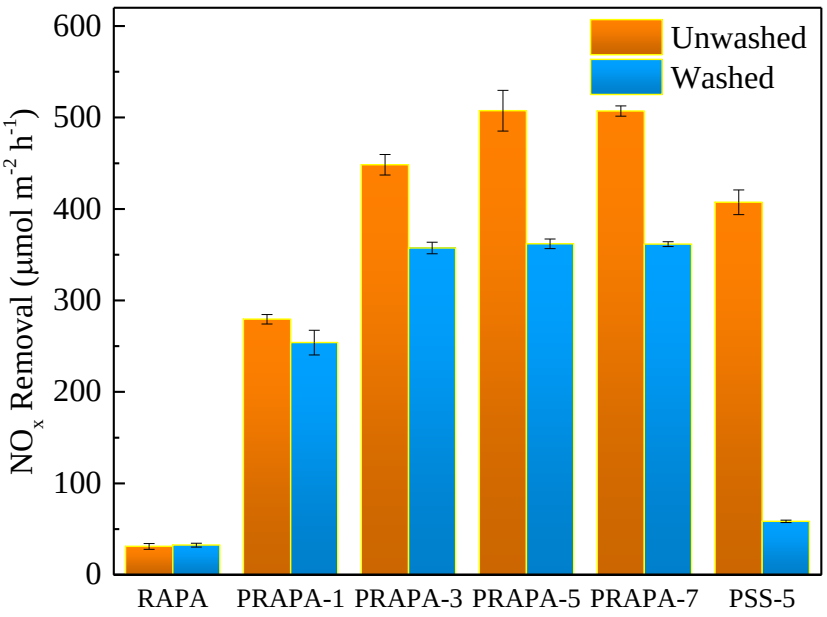

Figure 3.8 Photocatalytic NO_x removal of PSS-5 and PRAPA with different concentrations of CNNs suspensions before and after rain-wash.

The photocatalytic efficiency of PRAPA-7 is nearly constant with a further increase of CNNs concentration to 7 g L^{-1}. This is in line with nearly the same surface area of CNNs coatings on the surface of both PRAPA-5 and PRAPA-7 (Figure 3.6). This is reasonable against the background that with the further increasing concentration of CNNs from 5 g L^{-1} to 7 g L^{-1}, the overlap of CNNs will not significantly improve the photocatalytic efficiency because of the insufficient contact with light and pollutant [86, 107]. Hence, CNNs concentration of 5 g L^{-1} is considered the optimal CNNs concentration at which the highest cost effectiveness can be achieved. It should be pointed out that an increase in the photocatalytic efficiency of PRAPA does not result in a linear increase in the CNNs concentration. This can be explained by the overlap of CNNs even when CNNs concentration is less than 5 g L^{-1}. On the other hand, with the same CNNs concentration of 5 g L^{-1}, a decrease of 19.8% in photocatalytic efficiency is observed

in the PSS-5 compared to the PRAPA-5. This is attributable to the less content of CNNs on the surface of PSS-5 compared to PRAPA-5 (Figure 3.4 and Table 3.4).

To test the durability property, the PRAPA was subjected to the rain-wash. As shown in Table 3.5, the PSS-5 displays a remarkable decline in photocatalytic NO_x removal efficiency by nearly 85.7 % after the rain-wash due to massive loss of CNNs on the surface of SS (Table 3.3. This can be further confirmed by the SEM morphologies as observed in Figure 3.7. In cases of rain-wash, the reduction of photocatalytic efficiencies of PRAPA is less than 30% (Table 3.5). Specifically, the PRAPA-3 and PRAPA-5 as well as PRAPA-7 retain nearly the same NO_x removal efficiency of approximately 360 μmol m^{-2} h^{-1}, which is approximately 6 times higher than that of PSS-5. This is consistent with the remaining contents of CNNs (Table 3.4), because of strong washing resistance of PRAPA. These results clearly demonstrate that the RAPA is superior to SS as a substrate for photocatalyst due to the enhanced photocatalytic effect and washing resistance.

Table 3.5 Decline rate of photocatalytic NO_x removal efficiency of PSS-5 and PRAPA with different concentrations of CNNs suspensions after rain-wash (%).

	PRAPA-1	PRAPA-3	PRAPA-5	PRAPA-7	PSS-5
Decline rate	9.1	22.5	28.7	28.7	85.7

In practice, the PRAPA will be applied to the exposed aggregate cementitious materials. The photocatalytic NO_x removal activities of the PEACM prepared with PRAPA/PSS are shown in Figure 3.9.

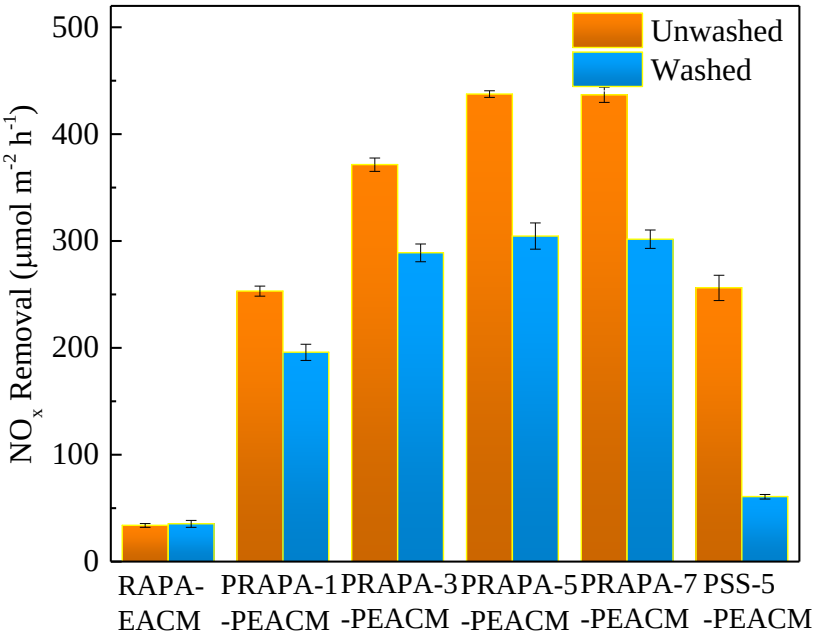

Figure 3.9 Photocatalytic NO_x removals of PEACM before and after rain-wash.

Before exposure to rain-wash, all the PEACM exhibit sufficient NO_x removal under visible light irradiation, in spite of a reduction in NO_x removal compared with PRAPA. This is attributed to the decrease of contact areas of CNNs coatings accessible to air pollutant and light. The photocatalytic NO_x removal efficiency of PRAPA-based PEACM increases first with increasing concentration of CNNs and then becomes almost constant. This behavior is in accordance with the photocatalytic efficiency of PRAPA. The PRAPA-5-PEACM and PRAPA-7-PEACM have a NO_x removal of approximately 437.0 μmol m^{-2} h^{-1}, which is considerably higher than that of PSS-5-PEACM (256.1 μmol m^{-2} h^{-1}). This may be attributed to the fact that the hydration products in the cementitious materials as opposed to PRAPA can envelop the hydrophilic surface of PSS more easily. All PRAPA-based PEACM retain a considerable photocatalytic effect after exposure to the rain-wash due to excellent washing resistance of

PRAPA, an expected observation. Whereas, the rain-wash causes a significant loss of photocatalytic efficiency in PSS-5-PEACM, drastically decreasing from 256.1 to 60.7 μmol m^{-2} h^{-1}. Specifically, the photocatalytic NO_x removal efficiency (approximately 300.0 μmol m^{-2} h^{-1}) of the PRAPA-5-PEACM is approximately 5 times higher than that of PSS-5-PEACM after exposure to the rain-wash. The results point to a great potential for application of the PRAPA-based PEACM, and provide a new route for preparation of highly cost-effective photocatalytic building materials.

3.4. Conclusions

Based on the adhesion and hydrophobicity properties of residual asphalt, the g-C_3N_4 nanosheets-recycled asphalt pavement aggregate composites have been prepared and applied in PEACM for an enhanced washing resistance. Major findings can be summarized below:

1) With a higher concentration of CNNs suspension, the photocatalytic NO_x removal efficiency of PRAPA increases first and then tends to be constant due to the limited surface area of RAPA.
2) The CNNs amount and photocatalytic NO_x removal efficiency are higher in PRAPA-5 than in PSS-5, while the CNNs loss rate of PRAPA-5 is remarkably lower than that of PSS-5 when subjected to rain wash. After rain wash, the NO_x removal efficiency of PRAPA-5 is found approximately 6 times higher than that of PSS-5.
3) The photocatalytic effect of PEACM corresponds well with that of PRAPA/PSS in spite of a slight reduction in photocatalytic activity. The PRAPA-based PEACM holds a remarkably stronger rain-wash resistance than the PSS-based PEACM.

CHAPTER 4 EFFICIENCY AND DURABILITY OF G-C_3N_4-BASED COATINGS APPLIED ON MORTAR UNDER PEELING AND WASHING TRIALS

4.1 Introduction

The hole-electron pairs produced from photocatalyst under sunlight irradiation can degrade organic [108, 109] and inorganic [110, 111] contaminants as well as microorganism [112, 113] in the presence of water and oxygen. Nitrogen oxides (NO_x) are the major pollutants that strongly induce environmental problems such as urban smog, acid rains and depletion of tropospheric ozone [114, 115]. It has been well demonstrated that the NO is oxidized first to NO_2 and then to HNO_3 by the light activated holes and associated active species such as superoxide ($\cdot O_2^-$) and hydroxyl radicals ($\cdot OH$) [116-119].

Titanium dioxide (TiO_2) is the most used photocatalyst in photocatalytic building materials due to its high chemical stability and relatively low price [120, 121]. Nonetheless, TiO_2 suffers from disadvantages such as low exploitation of sunlight because of its relatively large band gap (3.2 eV) [122] and fast recombination of photoinduced electron-holes [123, 124]. These somewhat impede its application. Graphitic carbon nitride (g-C_3N_4), also known as nontoxic metal-free materials, has emerged as an attractive photocatalyst with a visible-light driven bandgap (2.7 eV) and proper band edges [125, 126]. Over the past decade, g-C_3N_4 has been extensively studied for environmental pollution mitigation and renewable energy generation [127]. For instance, g-C_3N_4, typically prepared by the polycondensation of organic precursors containing both carbon and nitrogen, exhibits an effective photodegradation of organic pollutants and NO_x abatement under visible light irradiation [128, 129]. Therefore, the g-C_3N_4 could be a

promising alternative photocatalyst used in building materials.

The photocatalysts in the internal structure have difficulty participating in the photo-induced reactions, leading to a high cost but low efficiency of these photocatalyst products [130, 131]. The photocatalytic coatings prepared by spray coating [132, 133], dip-coating [134] and electrospray coating [135] have been developed to apply the uniformly dispersed photocatalyst onto the substrate surface. To date, although considerable progress on photocatalytic coatings mainly applied on stone and glass has been achieved in the recent years [135], the underlying mechanism of the coating application on stone or glass may not be applicable to cementitious materials due to their inherent characteristics such as high alkalinity and complex ion circumstances (Ca^{2+}, Na^{+}, OH^{-}). The research on the photocatalytic coating applied to cementitious materials is still at an infant stage, and previous reports mostly focused on optimizing photocatalytic efficiency of the photocatalytic products over improving their durability in real service conditions. The durability of the coatings is a crucial concern for large-scale applications.

Hassan and co-workers [136] may be the first to evaluate the durability and resistance to wear of TiO_2 surface coating applied on concrete pavement. Since then researchers are aware of the importance of considering the durability of photocatalytic building materials and release of photocatalyst particles [137, 138]. Maury-Ramirez and co-workers [139] investigated the weathering resistance of TiO_2 coating on autoclaved aerated concrete through a dip-coating, and found a decline in TiO_2 content by more than 93% after intensive weathering. The loss of the photocatalyst from coatings caused by wearing and water flow (rainfall) results in a reduction of photocatalytic activity and service life [140, 141] as well as an increase in health damage risk to humans [142, 143].

For immobilization of the catalyst on the substrate against rain-wash and abrasion in practical service conditions, various kinds of binders including acrylic resin [144], polyethersulfone [145] and fluoropolymer [146] have generally been added in these coatings. Vinyl ester is notable as an additive and has been widely used in coatings and adhesives with excellent resistance to a wide variety of commonly encountered environments [147]. There are two main approaches for fabricating the photocatalytic coatings incorporated with binder additives. First, catalyst powders are directly dispersed into the binder suspension to form a homogeneous composite sol for spraying or brushing process. Russa and co-workers [148, 149] developed TiO_2 coatings for cultural heritage protection and reported a nano-TiO_2 coating with desirable hydrophobicity, durability and self-cleaning properties, which was prepared by brushing the acrylic water suspension mixed with TiO_2. Secondly, an intermediate layer of the binder is applied on the substrate before installation of the photocatalytic layer. Persico and co-workers [150] developed a multilayered transparent fluoropolymeric coating applied on the quartz sheath for degradation of hydrosoluble pollutants, and the perfluorinated amorphous polymer that acts as a hydrophobic primer coating can not only improve the adhesion between the latter photoactive layer and the quartz, but also prevent water penetration. The SiO_2 layer was applied on cement substrate before the TiO_2 layer was sprayed, leading to an improved adhesion for TiO_2 coatings and a protective layer for substrate [151]. These organic-inorganic hybrid coatings, however, were developed and investigated mainly in laboratory conditions. Few reports on the resistance to wear and rain wash of these hybrid coatings applied to mortar substrate is available [152, 153].

From a literature survey, little effort has been devoted to optimizing the method of binder addition technique in term of efficiency and durability when preparing photoactive coating on the

mortar surface. In this chapter, the mortars were coated with two novel visible light-responsive coatings composed of vinyl chloride/vinyl ester/ethylene copolymer (as a binder) and g-C_3N_4. First, the binder suspension mixed with g-C_3N_4 was sprayed on the mortar to form the coating. Secondly, the binder water suspension is applied on mortar surface before the g-C_3N_4 suspension is sprayed. The g-C_3N_4 suspension without binder is sprayed on mortar as a control group. Under a peeling action and a simulated rain-wash process, the durability of these coated mortars was evaluated in view of g-C_3N_4 loss from the mortar surface by qualitative-quantitative SEM-EDS analysis. Hydrophobicity of these coated mortars is monitored by water contact angle measurements. The photocatalytic performances of the coated mortars were assessed in terms of NO_x removal under visible light before and after the durability tests (i.e. peeling test and washing test). This work provides a good reference for optimizing the efficiency and durability of the mortars with photocatalytic coatings.

4.2 Experimental

4.2.1 Materials and mortar substrate

Sinopharm Chemical Reagent Co. Ltd. provided urea without further purification. The binder was mainly composed of vinyl chloride/vinyl ester/ethylene copolymer. The characteristics of the binder are listed in Table 4.1. A grade of 42.5 R Portland cement was used. Deionized water was used throughout the experiments. The mortar substrate was fabricated with a constant mix proportion of water: cement: sand as 0.5: 1: 3 by mass. The fresh mortars were cast in the specific discs (Φ30 mm × 15 mm) and compacted carefully on a vibration table. Afterward, all the specimens were demolded after 24 hours, and then transferred into a curing chamber (20 °C and 98% relative humidity) for another 27 days. Preparation of g-C_3N_4 has been described in detail in subsection 2.2.2 [154].

Table 4.1 Characteristics of the binder (vinyl chloride/vinyl ester/ethylene copolymer).

Dynamic Viscosity (mPa·s)	Solid Content (%)	PH Value	Density (kg/m^3)
80~120	52 ± 1	7~9	1.1

4.2.2 Coating deposition

Two different procedures including mono-layer coating (MC) technique and double-layer coating (DC) technique were applied on the mortar to prepare the g-C_3N_4-based coatings. A diagram for illustrating the preparation process is shown in Figure 4.1. The binder was completely dissolved in deionized water via vigorous stirring at room temperature for 1 hour and became a homogeneous binder suspension (1 wt%). The g-C_3N_4 suspensions A and B (15 g L^{-1}) were obtained via 2 hours' sonication of the g-C_3N_4 powders in deionized water and in the binder suspension, respectively. The g-C_3N_4 suspension B was directly sprayed on the mortar to a monolayered g-C_3N_4-based coating mortar, denoted as MCM. To prepare the mortar coated with double-layered g-C_3N_4-based coatings, the binder suspension was first sprayed on the surface of mortar, and then dried at ambient temperature for 3 min before spraying the g-C_3N_4 suspension A, denoted as DCM (double-layer g-C_3N_4-based coating mortar). For both MCM and DCM, approximately 0.7 mg cm^{-2} of binder was applied on each sample. The g-C_3N_4 suspension A was sprayed on the mortar as a control sample. After coating, the coated mortars were dried for 24 h in a controlled laboratory environment (25 ± 2 ℃ and 30 ± 5% RH) and stored in dark conditions. For all the coated mortars, approximately 1.0 mg cm^{-2} of g-C_3N_4 was applied.

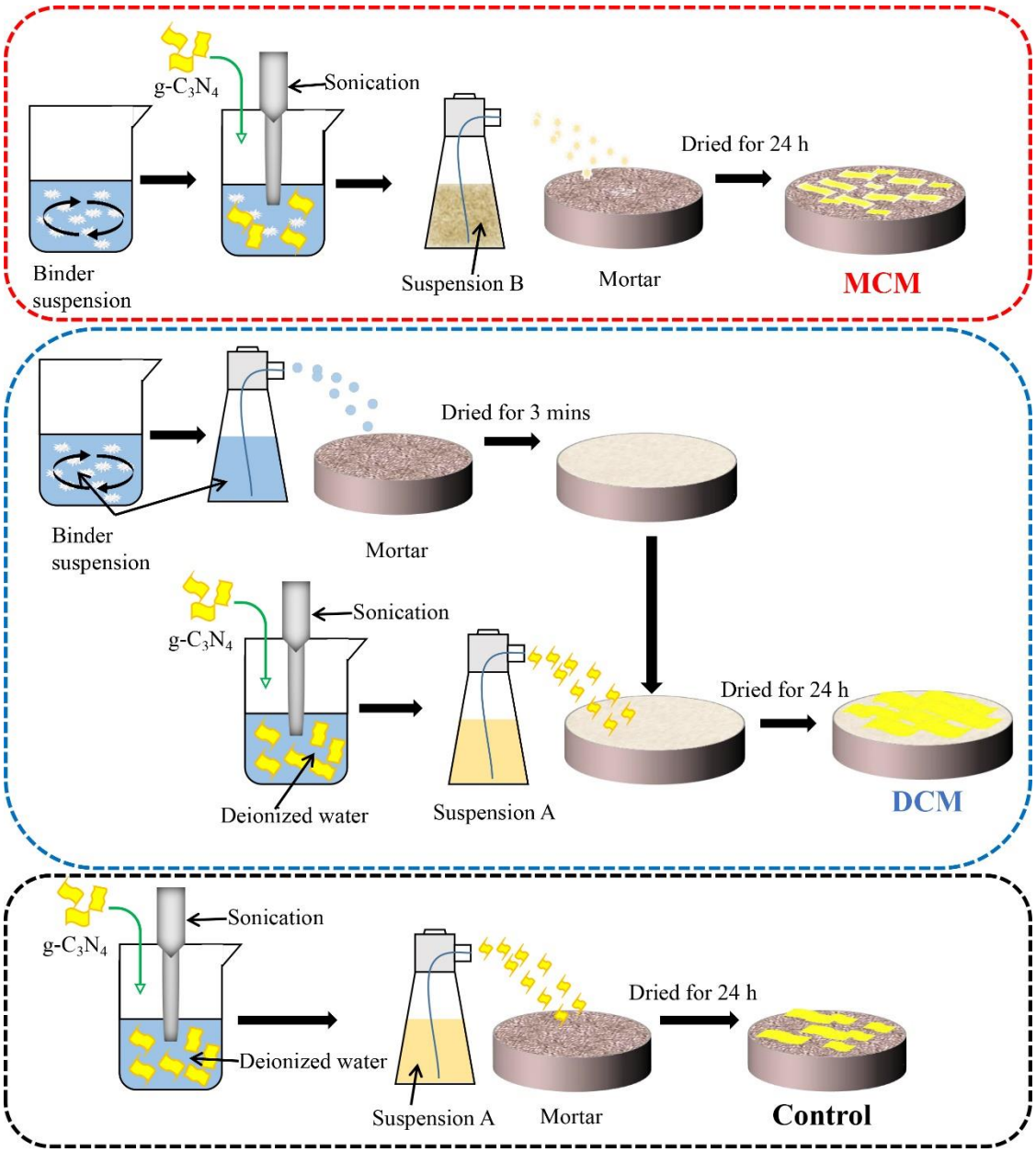

Figure 4.1 Schematic illustration on the preparation of the coated mortars.

4.2.3 Durability tests

The durability of the coated mortars was evaluated via peeling test and water wash process. The peeling experiment was performed according to a method reported previously, which was used for evaluating the surface cohesion of mortars and stones [155, 156]. In a typical process, a commercial adhesive tape (M&G Chenguang Stationery co., Ltd.) was stuck to the

surface of the coated mortar and smoothed with gentle finger pressure; after 10 seconds, the tape was removed rapidly. The test for each sample was repeated for a couple of times preassigned. New strips were used for each time.

The rain-wash is the most ubiquitous deterioration factor affecting the whole building facades and it is a primary concern for the durability of the coated mortar in real service conditions. The rain-wash process was simulated according to the set-up shown in Figure 3.2.

4.2.4 SEM-EDS analyses

Scanning Electron Microscopy (SEM) equipped with Energy-dispersive X-ray spectroscopy (EDS) (Bruker Quanta 250) was used to observe the morphology of the coatings on the mortars and to investigate the distribution of Nitrogen (noted as N hereafter) on the mortar surface. Comparative SEM observations and quantitative analyses of N by EDS were performed before and after the durability tests, to study the effect of the peeling action and the rain-wash process on the coated mortar. Morphological and elemental analyses were performed at an accelerated voltage of 15 kV. Distribution maps of element were acquired in Live Spectrum Mapping mode. The analytic time was 10 min for each EDS scan.

4.2.5 Contact angle measurements

Water contact angle (WCA) of the coated mortars was measured in order to evaluate the hydrophobicity of the coatings before and after the durability tests and after exposure to light/dark. A contact angle meter (OCA20, Dataphysics) was used to measure the WCAs. A water droplet (5 μL) was gently placed on the surface of the coated mortars using a microsyringe. Five locations on the coatings were chosen to measure the WCA and these were then averaged to report the equilibrium contact angle.

4.2.6 Photocatalytic NO_x removal test

The capability of air purification by the coated mortars was evaluated by photocatalytic NO_x abatement in a continuous reactor under visible light irradiation, based on a regular photocatalytic procedure ISO/DIS 22197-1. The schematic diagram of NO_x removal experimental set-up is shown already in Figure 2.5 [158]. Each test was repeated three times to obtain an average value. The amount of NO_x abatement was expressed as a subtraction of the NO_2 generated from the NO removed according to previous reports [131, 157]. The calculation of the amount of NO_x abatement can be referred to Equation (2.1).

4.3 Results and discussion

4.3.1 Microscopic observations

Figure 4.2 shows the microstructure of the coated mortars before the durability tests. The g-C_3N_4-based coatings can be observed clearly on all the samples, and mask the original surface morphology of the mortars. These coatings are consistent with EDS distribution maps where abundant C and N can be detected. The abundant cracks with raised edges can be observed on the control (Figure 4.2a). The obvious gaps between the mortar substrate and the coatings can also be found in the cross-sectional images (Figure 4.2d), suggesting a low anchorage of the coating to the mortar substrate. This can be explained by the fact that the g-C_3N_4 particles adhere to each other more strongly than their adhesion to the mortar substrate due to the high surface energy of the g-C_3N_4 particle. The MCM shows a smooth surface without visible crack (Figure 4.2b). This is attributed to the bonding effect of the intermixed binders between the g-C_3N_4 particles. Meanwhile, thanks to the adhesion of the binders, the coatings are attached tightly onto the mortars (Figure 4.2e), presenting a good anchorage of the coatings to the mortar substrate.

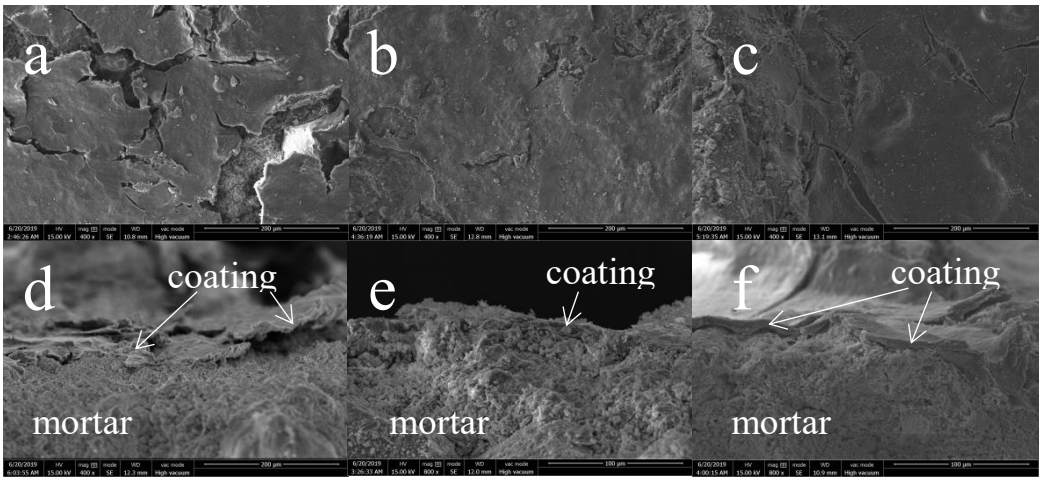

Figure 4.2 Morphologies of the coated mortar surfaces and cross sections: (a) and (d) control; (b) and (e) MCM; (c) and (f) DCM.

At higher magnifications (Figure s 4.3a and 4.3b), it is obvious that the g-C_3N_4 particles were covered by the amorphous binders compared to the identifiable g-C_3N_4 particles on the control. This corresponds well with the uniform distribution of Cl in the coatings. For the DCM (Figure 4.2c), the size of the micro cracks is smaller than that on the control, but larger than that on the MCM. This can be ascribed to the different distribution of the binders in the two samples. Compared to the uniformly distributed binders in the g-C_3N_4 layer (MCM), the insertion layer of the binders in the DCM only provided an anchoring effect for the bottom of the g-C_3N_4 layer. Hence, the cohesion of g-C_3N_4 particles still cause a few cracks on the g-C_3N_4 layer. Compared to the control with observable rough mortar substrate in the cracks, the smooth surface composed of binders is observed in the bottom of the micro cracks. This is in coincidence with the distribution of Cl on the surface of DCM. Additionally, the coatings on the DCM are stuck closely on the substrates, showing a good anchorage on the mortar surface. In the cross-sectional images (Figure 4.2f), the compatible binders attached compactly on the mortar were in close contact with the g-C_3N_4 layer, displaying a good bond between the g-C_3N_4 layer and the mortar substrate.

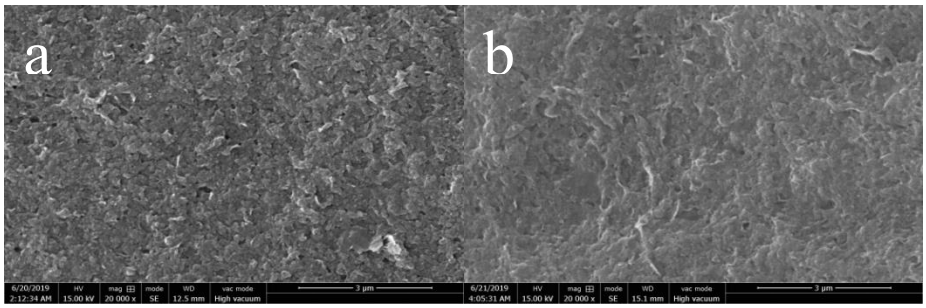

Figure 4.3 Surface morphologies of (a) control and (b) MCM at high magnifications.

Figure 4.4 shows the surface morphology of the control, MCM and DCM after 5 times of peeling action. For the control, the peeling action results in a large removal of the fissured coatings, leaving a rough surface morphology of the mortars and indicating a weak resistance to human touch. This can be attributed to the low adhesion of the mortar substrate. The MCM exhibits some rough mortar surface after peeling, while most coatings remained on the surface due to the improved adhesion from the intermixed binders. It has been reported that the intermixed binders can improve the wearing resistance and stability of the coatings on the substrate [159]. In case of the DCM, the surface morphology is almost unchanged after peeling in spite of a little exfoliation of the g-C_3N_4 layer, indicating a strong resistance to peeling. This can be attributed to the strengthened bonding effect provided by the binder layer between the mortar substrate and the g-C_3N_4 layer.

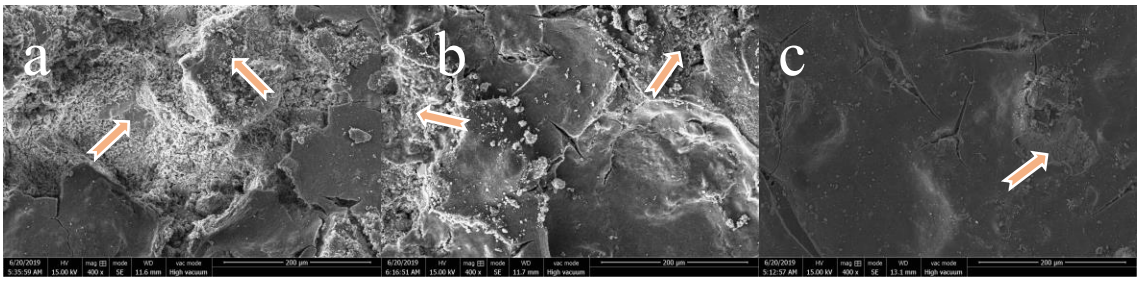

Figure 4.4 Surface morphologies of (a) control; (b) MCM and (c) DCM after peeling.

Figure 4.5 shows the microscopic morphologies for the control, MCM and DCM after 60

min washing. The control exhibits extensive rough surface of mortar substrate with few fragments of g-C_3N_4 layer (Figure 4.5a), indicating that the water washing has a severe impact on the coatings of the control, almost a complete loss of the coating. These findings demonstrate that the direct application of photocatalyst particles onto the mortar is not effective due to the weak resistance to washing and peeling. For the MCM, the larger area of g-C_3N_4 layer remained after washing compared to that on the control. This is attributed to the bonding effect of the intermixed binders, resulting in a better resistance to washing. It should be pointed out that the bonding effect of the intermixed binders in this MCM is limited due to the relatively low amount of intermixed binder. As a result, the CNNs coatings on the MCM were partially removed from the surface, leaving rough mortar surface when subjected to the simulated rain-wash (Figure 4.5b). As for the DCM, most g-C_3N_4 layers were still attached on the surface after washing, demonstrating a strong washing resistance. This can be attributed to the strong adhesion provided by binder layer. It is noteworthy that the larger cracks can be seen on the DCM after washing, suggesting that the main loss of g-C_3N_4 occurs at the discontinuous coating edge. The study on further optimization of the durability of the coated mortars is in progress to improve the continuity of the coating on the mortar.

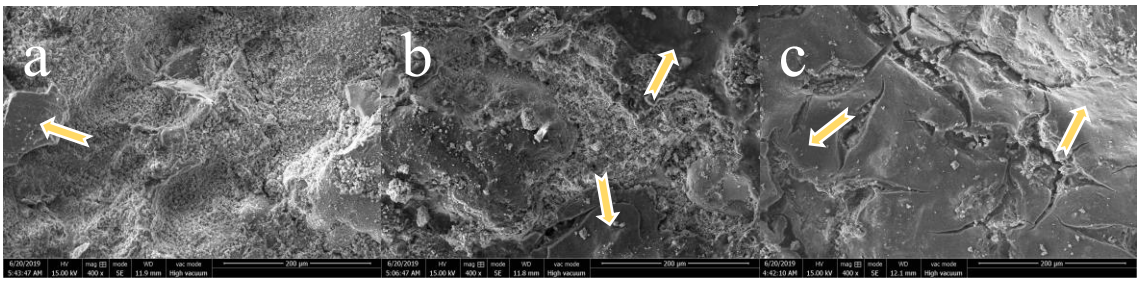

Figure 4.5 Surface morphologies of (a) control; (b) MCM and (c) DCM after 60 min washing.

In order to further investigate the effect of peeling and washing on the coated mortars, the EDS analysis was used to check the N content in the coatings before and after the durability

tests. The N signal can be regarded as coming from g-C_3N_4 attached on the surface of the coated mortar, and the N content measured on the surface of the coated mortars are reported in Table 4.2. The content of N recorded on the surface of coated mortars after the washing trial was remarkably lower than that after the peeling trial. Accordingly, the washing trial has a larger deterioration impact than the peeling trial. As expected, the control exhibits the lowest N content after peeling and washing, reduced by 59% and 79%, respectively. Due to the adhesion of the intermixed binders, the reduction of the N content on the MCM was smaller, 26% and 29 % respectively, than that of the control after peeling and washing. Meanwhile the remaining N content of MCM, which is higher than that of the control, drops from approximately 39.3% to 29.1% and 16.2%, corresponding to peeling test and washing test, respectively. More importantly, the DCM shows the least reduction in the N content after peeling and washing, about 15% and 21% respectively, and retains the highest content of N compared to the MCM and the control, indicating the strongest resistance to peeling and washing. As mentioned above, different treatments of binders have dramatically different effects on the durability of the coatings. Compared to the intermixed binder in the coating, a prior layer of binder contributes to the stronger resistance to coating exfoliation under peeling and washing trials.

Table 4.2 N content measured on the mortar surface (%).

	Before Durability tests	After 5 times of peeling	Δ	After 60 min of washing	Δ
Control	44.4 ± 5.4	18.1 ± 3.5	-59%	9.5 ± 2.2	-79%
MCM	39.3 ± 6.8	29.1 ± 6.3	-26%	16.2 ± 3.4	-59%
DCM	43.4 ± 4.6	37.1 ± 8.6	-15%	34.5 ± 6.7	-21%

4.3.2 Contact angle measurements

The wetting property of the coated mortars was investigated by the water contact angle (WCA) measurements. The results for MCM and DCM before and after durability tests are listed in Table 4.3. The WCA for the control cannot be detected, owing to the strong capillary water absorption of the mortar substrate and the fragmented g-C_3N_4 layer. Before the durability tests the WCA values of both MCM and DCM are higher than 80°, indicating an improved resistance to water penetration due to the inherent hydrophobic behavior of the binder. This is favorable for protecting the substrate from aggressive environmental hazards. After the durability tests, the WCA values of both MCM and DCM decrease slightly after the exfoliation of coatings, and the tested WCA value of DCM is clearly higher than that of MCM.

Table 4.3 Water contact angles of the coated mortars (°).

	Before durability tests	After 5 times of peeling	After 60 min of washing
Control	0	-	-
MCM	80.9 ± 3	70.3 ± 5	61.0 ± 6
DCM	83.1 ± 2	75.5 ± 6	70.1 ± 6

The change of the WCA after exposure to light/dark is further monitored. Figure 4.6 shows the results. After 4 hours of irradiation, the WCA value of MCM and DCM drastically decreases to 18.7° and 8.7 ± 5°, respectively, both exhibiting a hydrophilic surface. This can be attributed to the increase in hydroxyl-group concentration on the surface of the g-C_3N_4 in the presence of water molecules under light irradiation. It was reported [160] that the hydrophilicity induced by the photocatalyst under solar radiation can be responsible for the decrease in the contact angles in the mixture coatings. After keeping the sample in dark for 12 hours, the WCA value increases again, reaching 63.4 ± 10° and 67.2 ± 12° for DCM and MCM, respectively. This can be explained by the fact that the hydroxyl groups are slowly replaced by atmospheric oxygen

[161].

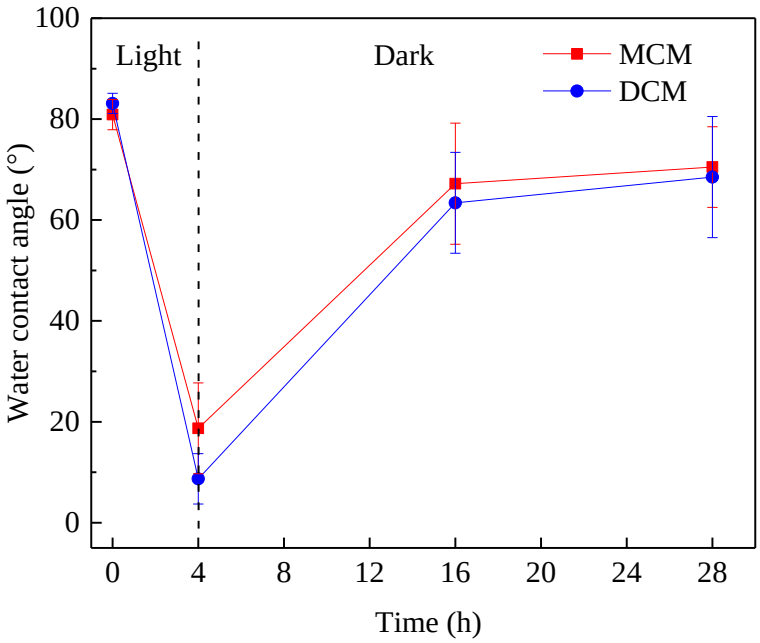

Figure 4.6 Change of WCA with exposure to light/dark.

4.3.3 Photocatalytic activity of the coated mortars

The photocatalytic performance of the coated mortars before and after subjecting to various degrees of peeling and washing is shown in Figures 4.7 and 4.8, respectively. Table 4.4 presents the loss rate of the NO_x removal efficiency of the coated mortars after 5 times of peeling and 60 min of washing. Before these durability tests, all the coated mortars show a highly efficient NO_x removal under visible light irradiation. This is reasonable given that the active species ($\cdot O_2^-$ and $\cdot OH$) formed on the g-C_3N_4 can oxidize NO_x to NO_3^- [162]. Among the three samples, the DCM presents the highest photocatalytic NO_x removal efficiency (283.9 μmol m^{-2} h^{-1}) than the control and the MCM. The MCM exhibits the lowest photocatalytic NO_x removal efficiency (230.8 μmol m^{-2} h^{-1}), caused by coverage of the g-C_3N_4 by the binders. This respect is

evidently supported by the observations from SEM image (Figure 4.4). The masking effect of the binders becomes pronounced with an increasing content of the binders due to the higher probability of g-C_3N_4 covered by binders, resulting in a remarkable decrease in the NO_x removal efficiency of MCM. This is in good agreement with the findings reported previously [163].

Table 4.4 Loss rate of the NO_x removal efficiency of the coated mortars after 5 times of peeling and 60 min of washing (%).

	After 5 times of peeling	After 60 min of washing
Control	56.8%	81.9%
MCM	34.1%	55.3%
DCM	18.1%	28.8%

As shown in Figure 4.7, with the increased times of peeling, the photocatalytic NO_x removal efficiency of all the coated mortars shows a decreasing trend. The control exhibits the largest decline about 56.8% compared to the MCM and DCM after 5 times of peeling action. This corresponds well with the large loss of g-C_3N_4 on the mortar surface due to the weak adhesion of the mortar substrate (Table 4.2). After 5 times of peeling action, the photocatalytic NO_x removal efficiency of the MCM is about 152.1 μmol m^{-2} h^{-1}, which is 33.3% higher that of the control (114.1 μmol m^{-2} h^{-1}). This is attributed to the fact that the intermixed binders are able to help preserve g-C_3N_4 particles on the surface. As for the DCM, the peeling action causes the least loss of photocatalytic performance (18.1%), dropping from 283.9 to 232.5 μmol m^{-2} h^{-1}. After 5 times of peeling action the DCM presents the highest photocatalytic NO_x removal efficiency, which is 2.0 and 1.5 times higher than that of the control and the MCM, respectively.

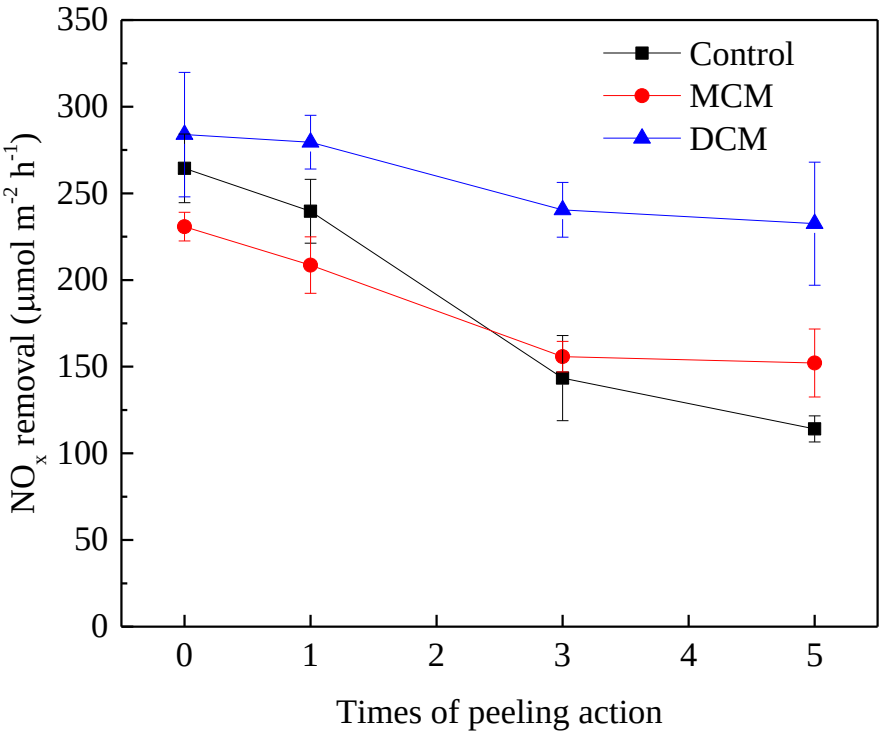

Figure 4.7 Photocatalytic NO_x removal efficiency of coated mortars subjected to peeling action.

The photocatalytic NO_x removal efficiency has decreased for all the coated mortars after exposure to the washing trials, as shown in Figure 4.8. With the increase of the washing time from 20 min to 60 min, a further decreasing trend of the photocatalytic NO_x removal efficiency is observed for all the samples. The control suffers an enormous reduction of about 81.9% in the NO_x removal efficiency after 60 min of washing, falling from 264.4 μmol m^{-2} h^{-1} to 47.8 μmol m^{-2} h^{-1}, suggesting a fragile resistance to washing. It is reasonable to consider that application of the photocatalyst without additives on the actual building surfaces is impracticable due to the weak stability of coatings and low long-term photocatalytic performance. For the MCM, distribution of the binder in the coatings can help to improve the bonding between g-C_3N_4 and mortar substrate. After 60 min of washing, the MCM shows a NO_x removal efficiency of 103.2 μmol m^{-2} h^{-1},

which is 2.1 times higher than that of the control. It is worth noting that the DCM exhibits the lowest loss of NO_x removal efficiency of about 28.8% compared to the MCM and the control when subjected to 60 min of washing action. In contrast, the DCM retains the highest NO_x removal efficiency of 202.1 μmol m^{-2} h^{-1}, which is in line with the highest N content observed above (Table 4.2), and it is 1.9 times and 4.2 times higher than that of the control and the MCM, respectively. Hence, a coating approach at which the highest NO_x removal efficiency of the coated mortars after peeling and washing are achieved is optimized. Furthermore, the relationship between photocatalytic NO_x removal efficiency and N content on the mortar surface is established, as shown in Figure 4.9. It can be observed that a linear relationship exists between the NO_x removal efficiency and the N content, with a regression coefficient R^2 of 0.987.

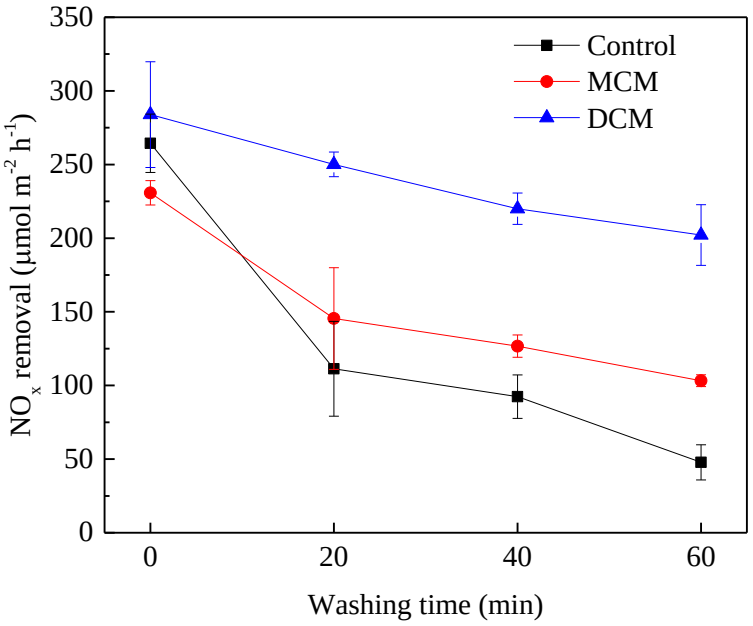

Figure 4.8 Photocatalytic NO_x removal efficiency of the coated mortars versus washing time.

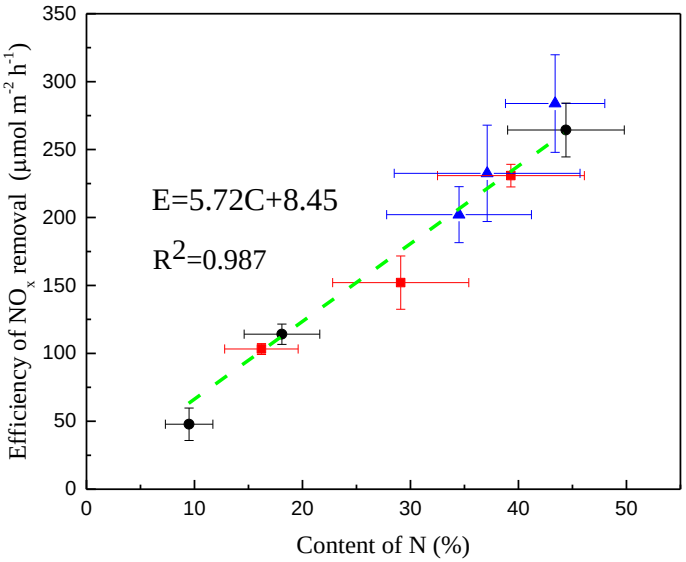

Figure 4.9 Relationship between photocatalytic NO_x removal efficiency and N content on the mortar surface.

4.4 Discussion

Application of photocatalyst as coating on the outdoor exposed building materials has been intensively developed for self-cleaning and depollution [164, 165]. Incorporation of the binder with photocatalyst, a type of hybrid coating, is an often-adopted approach to guarantee the long-term property of the photocatalytic coating in real service condition. [148, 160]. However, few reports on the durability of the hybrid coating applied to mortar substrates are available, and little effort has been devoted to optimizing the binder addition technique in term of efficiency and durability when preparing photoactive coating on the mortar surface. In this work, two binder addition techniques have been successfully applied to fabricate novel visible light-responsive coatings, composed of vinyl chloride/vinyl ester/ethylene copolymer and g-C_3N_4, on mortar surface. Their photocatalytic NO_x removal efficiency and resistance to peeling and washing are investigated and compared in detail.

Figure 4.10 illustrates the influence of different approaches of binder addition on the photocatalytic activity and durability of the coated mortars based on the above results. For the MCM, the intermixed binders are almost uniformly distributed in the g-C_3N_4-based layer. The binders distributed on the upper surface of the coatings are detrimental to the photocatalytic activity due to its masking effect that drastically weakens the contact of the g-C_3N_4 with the NO_x. The lowest NO_x removal efficiency before the durability tests is in the MCM compared with the control and the DCM. Due to the drying shrinkage, the control exhibits discontinuous coatings with large cracks, leading to a reduction in surface areas of the g-C_3N_4 coatings. This is detrimental to the photocatalytic reaction. While the DCM presents smooth coatings with smaller crack due to the good adhesion provided by the pre-inserted binder layer. As a result, the initial photocatalytic NO_x removal efficiency of the DCM is higher than that of the control.

Previous studies [156, 166] on durability of TiO_2 coatings applied on different substrates have shown the high surface roughness of substrate along with good durability of the photoactive coating due to the favorable adhesion of the substrate. Nonetheless, the aggressive peeling and washing actions can cause a significant loss of g-C_3N_4 layer on the control in spite of its sufficiently rough surface. This demonstrates that the surface roughness of substrate holds limited role on the durability of the coatings against the mechanical effects of human touch and real rain, and the direct application of photocatalyst particles onto the mortar is inadvisable due to their poor durability.

For the MCM, the binders on the bottom of the coatings can contribute to the bonding effect between the mortar and the g-C_3N_4-based layer, resulting in a good resistance to peeling and washing. It is reasonable to consider that a bigger amount of binders on the bottom of the coatings, from the MCM with a larger content of binders, can provide more bonds between the

mortar and the g-C_3N_4-based layer. However, the increased content of the intermixed binders tends to cause a reasonable increase in the amount of binders on the upper surface of the coatings, resulting in a decline in the photocatalytic performance. It can then be deduced that the MCM with the stronger resistance to coating exfoliation under peeling and washing trials holds inevitably the lower photocatalytic efficiency. This partly impedes its large-scale application due to high cost and low efficiency.

As for the DCM, the double-layer structure takes full advantage of binder adhesion by employing an intermediate binder layer before construction of the g-C_3N_4 layer. The binder layer can provide sufficient adhesion for the g-C_3N_4 layer without compromising its photocatalytic efficiency, resulting in strong resistance to peeling and washing. What's more, the dosage of the binder layer can be increased to acquire desirable bonds between the mortar substrate and the g-C_3N_4 layer without any adverse impact on its photocatalytic activity. The proposed double-layer coating technique, which overcomes the contradiction between durability and efficiency in the conventional mono-layer coating, proved to fabricate durable photocatalytic coating on cementitious materials without compromising its photocatalytic efficiency. It should be pointed out that the intermediate binder layer only contributes to bonding effect on the bottom of the g-C_3N_4 layer. A few cracks occur accordingly on the surface of the g-C_3N_4 layer, which will be a potential source for loss of the coatings when subjected to the action of the peeling and washing. Improvements on the coating for uniformity without cracking to achieve better durability will be the subject of a further study.

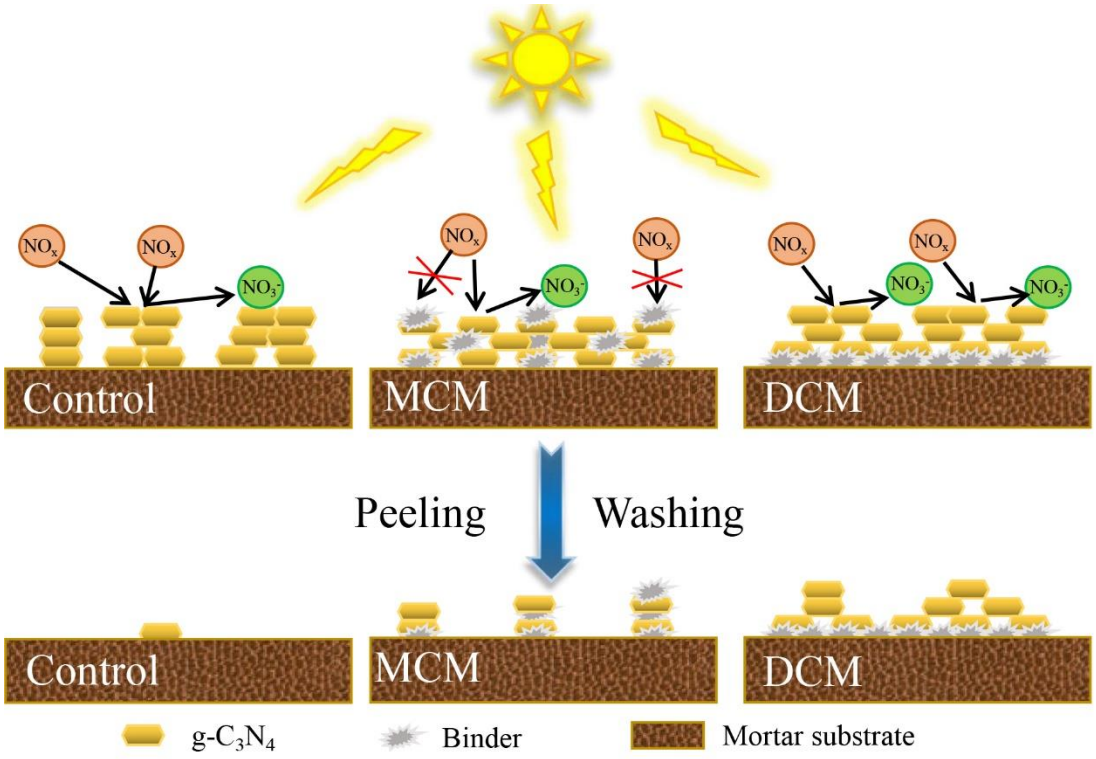

Figure 4.10 Schematic illustration of the photocatalytic activity and durability of the coated mortars fabricated by different approaches.

The primary objective of this article is to propose preliminary strategy to fabricate highly cost-effective and durable photocatalytic coatings applied on cementitious materials, and provide the information on the mechanical resistance to peeling and washing of these coatings. The durability assessment on surface carbonation and ageing of the proposed double-layer coating applied on cementitious materials is worthwhile to continue in detail for further study. The carbonation of cementitious materials is a universal phenomenon, where the formation of calcite via chemical reaction between calcium hydroxide in the cement paste and carbon dioxide (CO_2) from the air can block the surface of the catalyst [167]. The binder acts as a barrier that can sufficiently prevent the contact between the mortar surface and the CO_2 in the air. The binder in MC is usually randomly distributed and can be relatively poorly connected. The binder in DC, in contrast, is present as a whole on the mortar surface and is therefore well connected, as already

illustrated in Figure 4.10. In this sense, the resistance to CO_2 ingress of the DC should be stronger than that of the MC. Moreover, in the field of photocatalytic coatings, special effort should be paid to the well-known issue that polymeric binder can be degraded in the process of photocatalysis. The photocatalysis occurs primarily on the surface of the coating that is accessible to the light. In the MC, the oxidative species ($\cdot O_2^-$ and $\cdot OH$) formed on the surface are prone to degrade the binder around the surface. As for the DC, the oxidative species need to pass through the g-C_3N_4 layer to degrade the binder layer. In this penetration process, the oxidative species may be partly consumed. What's more, the g-C_3N_4 layer provides a shield for the binder layer to protect against UV radiation. Consequently, the resistance of DC to ageing can be stronger than that of MC. In addition, by increasing the thickness of g-C_3N_4 layer in the coating, the photo-induced degradation of the binder layer can reasonably be decreased. A more detailed and complete experimental study is in the stage of development to provide a solid validation for the more durable behaviors of the DC when used in real engineering practice.

4.5 Conclusions

Two novel visible light-responsive coatings composed of vinyl chloride/vinyl ester/ethylene copolymer and g-C_3N_4, which are applied on mortar surface, have been developed by two binder addition techniques including mono-layer coating (MC) technique and double-layer coating (DC) technique, respectively. The g-C_3N_4 suspension without binder is sprayed on mortar as a control group. The coated mortars hold efficient NO_x removal efficiency under visible light irradiation and desirable hydrophobicity. Major findings can be summarized below:

1) In spite of high surface roughness of mortar, the control exhibits discontinuous coatings with large crack due to the drying shrinkage, showing a low anchorage to mortar substrate. This can be responsible for the week resistance to peeling and washing.

2) Compared to the control, the MC and DC mortars present a better anchorage to mortar substrate due to the adhesion of the binder, along with a better resistance to peeling and washing. The addition of binder accounts for the hydrophobicity of MC and DC mortars.
3) Before the durability tests (i.e. peeling test and washing test), the MC mortar exhibits the lowest photocatalytic efficiency compared to both the control and the DC mortar due to the masking effect of the intermixed binder. The MC mortar with higher amount of binder has the lower photocatalytic efficiency, which impedes its practical application due to the high cost and low effectiveness.
4) Contradiction between durability and efficiency often exists in the conventional MC. The proposed DC technique, which overcomes that contradiction, proved to fabricate durable photocatalytic coating on cementitious materials without compromising its photocatalytic efficiency.

CHAPTER 5 CONCLUSIONS AND PROSPECTS

To address the environmental and durability issues associated with the use of nano-TiO_2 in concrete, this work focused on developing an environmentally friendly and durable cementitious system based on synergistic activities of multifunctional photocatalytic Graphitic carbon nitride (g-C_3N_4).

The photocatalytic cementitious composites (PCC) were prepared in three different approaches:

(1) Incorporating g-C_3N_4 nanosheets (CNNs) in Portland cement at three mixing dosages (0.5%, 1% and 2% by weight of cement).

(2) Applying CNNs suspension at various concentration levels as the coating on recycled asphalt pavement aggregate (RAPA).

(3) Applying CCNs suspension with vinyl chloride/vinyl ester/ethylene copolymer (as a binder) as the coating on cement mortar.

The photocatalytic performance and durability of the newly developed photocatalytic cementitious composites were evaluated systematically. For the first approach, it was found that a moderate amount of CNNs (below 2%) in cementitious composites was effective in achieving an improved photocatalytic depollution and self-cleaning performance under visible light. The second approach found that the cohesive property of residual asphalt is beneficial to the attachment CNNs on the surface of RAPA due to a strong bond between CNNs and RAPA. Compared to the CNNs-standard sand cementitious composites, the photocatalytic exposed aggregate cementitious materials (PEACM) showed the higher photocatalytic activity and better resistance to rain-wash. For the third approach, two types of coating methods were applied with

CNNs/binder on mortar surface, i.e., mono-layer coating (MC) and double-layer coating (DC). Results show that the binder addition leads to a good anchorage of the g-C_3N_4-based coatings on both MC and DC mortar substrates, along with desirable resistance to peeling and washing, compared to the g-C_3N_4 coated mortar without the binder. The well-distributed binder in g-C_3N_4-based coating inevitably decreases the photocatalytic efficiency of the MC mortar due to masking effect of the binder on the coating surface. The DC mortar, on the contrary, takes full advantage of the binder adhesion by inserting a binder layer and therefore holds strong resistance to peeling and washing without compromising its photocatalytic efficiency.

While this work mainly showcases the photocatalytic behavior and durability of the cementitious composites with CNNs, the obtained knowledge sheds light on future possibilities for developing a novel systematic strategy towards air-purifying, corrosion resistant, and self-healing concrete infrastructure. In particular, the future work is expected to manipulate cement chemistry and implement a molecular immobilization mechanism of g-C_3N_4 within a multifunctional host composite, e.g. Layered Double Hydroxide (LDHs). In addition to g-C_3N_4-LDH, synthetic microcapsules of various sizes and tunable mechanical properties containing healing agent will be applied synergistically for self-healing purpose.

REFERENCES

[1] M. Pérez-Nicolás, I. Navarro-Blasco, J.M. Fernández, J.I. Alvarez, Atmospheric NO_x removal: study of cement mortars with iron-and vanadium-doped TiO_2 as visible light–sensitive photocatalysts, Constr. Build. Mater. 149 (2017) 257-271.

[2] J. Ângelo, L. Andrade, L.M. Madeira, A. Mendes, An overview of photocatalysis phenomena applied to NO_x abatement, J. Environ. Manage. 129 (2013) 522-539.

[3] M. Pérez-Nicolás, J. Balbuena, M. Cruz-Yusta, L. Sánchez, I. Navarro-Blasco, J. Fernández, J. Alvarez, Photocatalytic NO_x abatement by calcium aluminate cements modified with TiO_2: Improved NO_2 conversion, Cem. Concr. Res. 70 (2015) 67-76.

[4] A. Aziz, K.S. Kim, Synergistic effect of UV pretreated Fe-ZSM-5 catalysts for heterogeneous catalytic complete oxidation of VOC: a technology development for sustainable use, J. Hazard. Mater. 340 (2017) 351-359.

[5] M.-Z. Guo, T.-C. Ling, C.-S. Poon, Nano-TiO_2-based architectural mortar for NO removal and bacteria inactivation: Influence of coating and weathering conditions, Cem. Concr. Compos. 36 (2013) 101-108.

[6] M.V. Diamanti, R. Paolini, M. Rossini, A.B. Aslan, M. Zinzi, T. Poli, M.P. Pedeferri, Long term self-cleaning and photocatalytic performance of anatase added mortars exposed to the urban environment, Constr. Build. Mater. 96 (2015) 270-278.

[7] T. Martinez, A. Bertron, E. Ringot, G. Escadeillas, Degradation of NO using photocatalytic coatings applied to different substrates, Build. Environ. 46(9) (2011) 1808-1816.

[8] J. Ângelo, L. Andrade, A. Mendes, Highly active photocatalytic paint for NO_x abatement under real-outdoor conditions, Appl. Catal. A 484 (2014) 17-25.

[9] M.-Z. Guo, C.-S. Poon, Photocatalytic NO removal of concrete surface layers intermixed with TiO_2, Build. Environ. 70 (2013) 102-109.

[10] A.M. Ramirez, K. Demeestere, N. De Belie, T. Mäntylä, E. Levänen, Titanium dioxide coated cementitious materials for air purifying purposes: preparation, characterization and toluene removal potential, Build. Environ. 45(4) (2010) 832-838.

[11] A. Calia, M. Lettieri, M. Masieri, S. Pal, A. Licciulli, V. Arima, Limestones coated with photocatalytic TiO_2 to enhance building surface with self-cleaning and depolluting abilities, J. Clean. Prod. 165 (2017) 1036-1047.

[12] T. Vulic, O. Rudic, S. Vucetic, D. Lazar, J. Ranogajec, Photocatalytic activity and stability of TiO_2/ZnAl layered double hydroxide based coatings on mortar substrates, Cem. Concr. Compos. 58 (2015) 50-58.

[13] D. Macphee, A. Folli, Photocatalytic concretes—The interface between photocatalysis and cement chemistry, Cem. Concr. Res. 85 (2016) 48-54.

[14] F. Rodriguez-Rivas, A. Pastor, C. Barriga, M. Cruz-Yusta, L. Sánchez, I. Pavlovic, Zn-Al layered double hydroxides as efficient photocatalysts for NO_x abatement, Chem. Eng. J. 346 (2018) 151-158.

[15] Shi, X., Veneziano, D., Xie, N., Gong, J. Use of chloride-based ice control products for sustainable winter maintenance: A balanced perspective. Cold Reg Sci Technol, 86 (2013) 104-112.

[16] Koch, G.H., Brongers, M.P., Thompson, N.G., Virmani, Y.P., Payer, J.H. Corrosion cost and preventive strategies in the United States, Report FHWA-RD-01-156 prepared for FHWA, Office of Infrastructure Research and Development, 2002.
[17] Yan, D., Wei, M. (Eds.). Photofunctional Layered Materials (Vol. 166), Springer, 2015.
[18] Yang, Z, Fischer, H., Polder, R. Modified hydrotalcites as a new emerging class of smart additive of reinforced concrete for anticorrosion applications: A literature review, Mater. Corros. 64 (2013) 1066-1074.
[19] X. Wang, K. Maeda, A. Thomas, K. Takanabe, G. Xin, J.M. Carlsson, K. Domen, M. Antonietti, A metal-free polymeric photocatalyst for hydrogen production from water under visible light, Nat. Mater. 8(1) (2009) 76-80.
[20] D.J. Martin, K. Qiu, S.A. Shevlin, A.D. Handoko, X. Chen, Z. Guo, J. Tang, Highly efficient photocatalytic H_2 evolution from water using visible light and structure-controlled graphitic carbon nitride, Angew. Chem. Int. Ed. 53(35) (2014) 9240-9245.
[21] R. Kuriki, K. Sekizawa, O. Ishitani, K. Maeda, Visible-light-driven CO_2 reduction with carbon nitride: enhancing the activity of ruthenium catalysts, Angew. Chem. Int. Ed. 54(8) (2015) 2406-2409.
[22] G. Mamba, A. Mishra, Graphitic carbon nitride (g-C3N4) nanocomposites: a new and exciting generation of visible light driven photocatalysts for environmental pollution remediation, Appl. Catal. B 198 (2016) 347-377.
[23] W.-J. Ong, L.-L. Tan, Y.H. Ng, S.-T. Yong, S.-P. Chai, Graphitic carbon nitride ($g\text{-}C_3N_4$)-based photocatalysts for artificial photosynthesis and environmental remediation: are we a step closer to achieving sustainability, Chem. Rev. 116(12) (2016) 7159-7329.
[24] F. Chang, C. Li, J. Luo, Y. Xie, B. Deng, X. Hu, Enhanced visible-light-driven photocatalytic performance of porous graphitic carbon nitride, Appl. Surf. Sci. 358 (2015) 270-277.
[25] I. Papailias, T. Giannakopoulou, N. Todorova, D. Demotikali, T. Vaimakis, C. Trapalis, Effect of processing temperature on structure and photocatalytic properties of g-C3N4, Appl. Surf. Sci. 358 (2015) 278-286.
[26] T. Sano, S. Tsutsui, K. Koike, T. Hirakawa, Y. Teramoto, N. Negishi, K. Takeuchi, Activation of graphitic carbon nitride ($g\text{-}C_3N_4$) by alkaline hydrothermal treatment for photocatalytic NO oxidation in gas phase, J. Mater. Chem. A 1(21) (2013) 6489-6496.
[27] P. Niu, L. Zhang, G. Liu, H.M. Cheng, Graphene-like carbon nitride nanosheets for improved photocatalytic activities, Adv. Funct. Mater. 22(22) (2012) 4763-4770.
[28] K. Schwinghammer, M.B. Mesch, V. Duppel, C. Ziegler, J.r. Senker, B.V. Lotsch, Crystalline carbon nitride nanosheets for improved visible-light hydrogen evolution, J. Am. Chem. Soc. 136(5) (2014) 1730-1733.
[29] F. Peng, Y. Ni, Q. Zhou, J. Kou, C. Lu, Z. Xu, New g-C3N4 based photocatalytic cement with enhanced visible-light photocatalytic activity by constructing muscovite sheet/SnO2 structures, Constr. Build. Mater. 179 (2018) 315-325.
[30] X. Lu, K. Xu, P. Chen, K. Jia, S. Liu, C. Wu, Facile one step method realizing scalable production of g-C3N4 nanosheets and study of their photocatalytic H2 evolution activity, J. Mater. Chem. A 2(44) (2014) 18924-18928.
[31] D.F. Aponte, M. Barra, E. Vàzquez, Durability and cementing efficiency of fly ash in concretes, Constr. Build. Mater. 30 (2012) 537-546.

[32] I.F. Olmo, E. Chacon, A. Irabien, Influence of lead, zinc, iron (III) and chromium (III) oxides on the setting time and strength development of Portland cement, Cem. Concr. Res. 31(8) (2001) 1213-1219.
[33] G. Bernardo, A. Telesca, G.L. Valenti, A porosimetric study of calcium sulfoaluminate cement pastes cured at early ages, Cem. Concr. Res. 36(6) (2006) 1042-1047.
[34] R.A. Cook, K.C. Hover, Mercury porosimetry of hardened cement pastes, Cem. Concr. Res. 29(6) (1999) 933-943.
[35] B. Das, P.K. Eswar, U. Ramamurty, C.N. Rao, Nano-indentation studies on polymer matrix composites reinforced by few-layer graphene, Nanotechnology 20(12) (2009) 125705.
[36] P. Hou, S. Kawashima, D. Kong, D.J. Corr, J. Qian, S.P. Shah, Modification effects of colloidal nanoSiO2 on cement hydration and its gel property, Compos. Part B 45(1) (2013) 440-448.
[37] M.-Z. Guo, C.S. Poon, Superior photocatalytic NOx removal of cementitious materials prepared with white cement over ordinary Portland cement and the underlying mechanisms, Cem. Concr. Compos. 90 (2018) 42-49.
[38] J. Chen, S.-c. Kou, C.-s. Poon, Photocatalytic cement-based materials: Comparison of nitrogen oxides and toluene removal potentials and evaluation of self-cleaning performance, Build. Environ. 46(9) (2011) 1827-1833.
[39] H. Du, S. Dai Pang, Dispersion and stability of graphene nanoplatelet in water and its influence on cement composites, Constr. Build. Mater. 167 (2018) 403-413.
[40] Z. Wu, C. Shi, K.H. Khayat, S. Wan, Effects of different nanomaterials on hardening and performance of ultra-high strength concrete (UHSC), Cem. Concr. Compos. 70 (2016) 24-34.
[41] K.L. Scrivener, A. Nonat, Hydration of cementitious materials, present and future, Cem. Concr. Res. 41(7) (2011) 651-665.
[42] C. Hesse, F. Goetz-Neunhoeffer, J. Neubauer, A new approach in quantitative in-situ XRD of cement pastes: Correlation of heat flow curves with early hydration reactions, Cem. Concr. Res. 41(1) (2011) 123-128.
[43] D. Jansen, F. Goetz-Neunhoeffer, B. Lothenbach, J. Neubauer, The early hydration of Ordinary Portland Cement (OPC): An approach comparing measured heat flow with calculated heat flow from QXRD, Cem. Concr. Res. 42(1) (2012) 134-138.
[44] V.V. Rocha, P. Ludvig, A.C.C. Trindade, F. de Andrade Silva, The influence of carbon nanotubes on the fracture energy, flexural and tensile behavior of cement based composites, Constr. Build. Mater. 209 (2019) 1-8.
[45] N.H. de Azevedo, P.J. Gleize, Effect of silicon carbide nanowhiskers on hydration and mechanical properties of a Portland cement paste, Constr. Build. Mater. 169 (2018) 388-395.
[46] B. Han, Q. Zheng, S. Sun, S. Dong, L. Zhang, X. Yu, J. Ou, Enhancing mechanisms of multi-layer graphenes to cementitious composites, Composites Part A 101 (2017) 143-150.
[47] Y. Qing, Z. Zenan, K. Deyu, C. Rongshen, Influence of nano-SiO2 addition on properties of hardened cement paste as compared with silica fume, Constr. Build. Mater. 21(3) (2007) 539-545.

[48] R. Ylmén, U. Jäglid, B.-M. Steenari, I. Panas, Early hydration and setting of Portland cement monitored by IR, SEM and Vicat techniques, Cem. Concr. Res. 39(5) (2009) 433-439.
[49] S.A.E. Aleem, M. Heikal, W. Morsi, Hydration characteristic, thermal expansion and microstructure of cement containing nano-silica, Constr. Build. Mater. 59 (2014) 151-160.
[50] M. Wu, Y. Zhang, Y. Jia, W. She, G. Liu, Z. Wu, W. Sun, Influence of sodium hydroxide on the performance and hydration of lime-based low carbon cementitious materials, Constr. Build. Mater. 200 (2019) 604-615.
[51] M.S. Kim, Y. Jun, C. Lee, J.E. Oh, Use of CaO as an activator for producing a price-competitive non-cement structural binder using ground granulated blast furnace slag, Cem. Concr. Res. 54 (2013) 208-214.
[52] I. Galan, L. Perron, F.P. Glasser, Impact of chloride-rich environments on cement paste mineralogy, Cem. Concr. Res. 68 (2015) 174-183.
[53] M.S. Lemos, A.L.C.D. Cunha, J. Dweck, A study of cement Type II hydration partially substituted by Brazilian spent cracking catalyst fines, J. Therm. Anal. Calorim. 130(1) (2017) 573-584.
[54] S. Cui, P. Liu, J. Su, E. Cui, C. Guo, B. Zhu, Experimental study on mechanical and microstructural properties of cement-based paste for shotcrete use in high-temperature geothermal environment, Constr. Build. Mater. 174 (2018) 603-612.
[55] X. Li, D. Chen, N. Li, Q. Xu, H. Li, J. He, J. Lu, One-step synthesis of honeycomb-like carbon nitride isotype heterojunction as low-cost, high-performance photocatalyst for removal of NO, ACS Sustainable Chem. Eng. 6(8) (2018) 11063-11070.
[56] J. Hu, D. Chen, N. Li, Q. Xu, H. Li, J. He, J. Lu, Fabrication of graphitic-C3N4 quantum dots/graphene-InVO4 aerogel hybrids with enhanced photocatalytic NO removal under visible-light irradiation, Appl. Catal., B 236 (2018) 45-52.
[57] B. Ruot, A. Plassais, F. Olive, L. Guillot, L. Bonafous, TiO2-containing cement pastes and mortars: measurements of the photocatalytic efficiency using a rhodamine B-based colourimetric test, Sol. Energy 83(10) (2009) 1794-1801.
[58] H.B. Singh, L.J. Salas, W. Viezee, Global distribution of peroxyacetyl nitrate, Nature 321 (1986) 588-591.
[59] H. Ren, P. Koshy, W.-F. Chen, S. Qi, C.C. Sorrell, Photocatalytic materials and technologies for air purification, J. Hazard. Mater. 325 (2017) 340-366.
[60] D. Seo, T.S. Yun, NOx removal rate of photocatalytic cementitious materials with TiO2 in wet condition, Build. Environ. 112 (2017) 233-240.
[61] M.-Z. Guo, A. Maury-Ramirez, C.S. Poon, Photocatalytic activities of titanium dioxide incorporated architectural mortars: Effects of weathering and activation light, Build. Environ. 94 (2015) 395-402.
[62] C. Cárdenas, J.I. Tobón, C. García, J. Vila, Functionalized building materials: Photocatalytic abatement of NOx by cement pastes blended with TiO2 nanoparticles, Constr. Build. Mater. 36 (2012) 820-825.
[63] M.-Z. Guo, J. Chen, M. Xia, T. Wang, C.S. Poon, Pathways of conversion of nitrogen oxides by nano TiO2 incorporated in cement-based materials, Build. and Environ. 144 (2018) 412-418.
[64] H.-J. Kim, Y.-S. Yoon, K.-H. Yang, S.-J. Kwon, Durability and purification performance of concrete impregnated with silicate and sprayed with photocatalytic TiO2, Constr. Build. Mater. 199 (2019) 106-114.

[65] E. Seftel, M. Niarchos, N. Vordos, J. Nolan, M. Mertens, A.C. Mitropoulos, E. Vansant, P. Cool, LDH and TiO2/LDH-type nanocomposite systems: A systematic study on structural characteristics, Microporous Mesoporous Mater. 203 (2015) 208-215.
[66] T. Yang, J. Peng, Y. Zheng, X. He, Y. Hou, L. Wu, X. Fu, Enhanced photocatalytic ozonation degradation of organic pollutants by ZnO modified TiO2 nanocomposites, Appl. Catal. B 221 (2018) 223-234.
[67] F. Rodriguez-Rivas, A. Pastor, C. Barriga, M. Cruz-Yusta, L. Sánchez, I. Pavlovic, Zn-Al layered double hydroxides as efficient photocatalysts for NOx abatement, Chem. Eng. J. 346 (2018) 151-158.
[68] A. Calia, M. Lettieri, M. Masieri, Durability assessment of nanostructured TiO2 coatings applied on limestones to enhance building surface with self-cleaning ability, Build. Environ. 110 (2016) 1-10.
[69] P. Niu, L. Zhang, G. Liu, H.M. Cheng, Graphene-like carbon nitride nanosheets for improved photocatalytic activities, Adv. Funct. Mater. 22 (2012) 4763–4770.
[70] G. Shi, L. Yang, Z. Liu, X. Chen, J. Zhou, Y. Yu, Photocatalytic reduction of CO2 to CO over copper decorated g-C3N4 nanosheets with enhanced yield and selectivity, Appl. Surf. Sci. 427 (2018) 1165-1173.
[71] Q. Lin, L. Li, S. Liang, M. Liu, J. Bi, L. Wu, Efficient synthesis of monolayer carbon nitride 2D nanosheet with tunable concentration and enhanced visible-light photocatalytic activities, Appl. Catal., B 163 (2015) 135-142.
[72] F. Dong, Y. Li, Z. Wang, W.-K. Ho, Enhanced visible light photocatalytic activity and oxidation ability of porous graphene-like g-C3N4 nanosheets via thermal exfoliation, Appl. Surf. Sci. 358 (2015) 393-403.
[73] P. Liu, Y. Gao, F. Wang, W. Zhang, L. Yang, J. Yang, Y. Liu, Photocatalytic activity of Portland cement loaded with 3D hierarchical Bi2WO6 microspheres under visible light, Constr. Build. Mater. 120 (2016) 42-47.
[74] E. Jimenez-Relinque, J. Rodriguez-Garcia, A. Castillo, M. Castellote, Characteristics and efficiency of photocatalytic cementitious materials: Type of binder, roughness and microstructure, Cem. Concr. Res. 71 (2015) 124-131.
[75] A. Zhao, J. Yang, E.-H. Yang, Self-cleaning engineered cementitious composites, Cem. Concr. Compos. 64 (2015) 74-83.
[76] W. Shen, C. Zhang, Q. Li, W. Zhang, L. Cao, J. Ye, Preparation of titanium dioxide nano particle modified photocatalytic self-cleaning concrete, J. Clean. Prod. 87 (2015) 762-765.
[77] A. Folli, C. Pade, T.B. Hansen, T. De Marco, D.E. Macphee, TiO2 photocatalysis in cementitious systems: Insights into self-cleaning and depollution chemistry, Cem. Concr. Res. 42(3) (2012) 539-548.
[78] S. Lucas, V. Ferreira, J.B. De Aguiar, Incorporation of titanium dioxide nanoparticles in mortars—Influence of microstructure in the hardened state properties and photocatalytic activity, Cem. Concr. Res. 43(43) (2013) 112-120.
[79] T. Martinez, A. Bertron, E. Ringot, G. Escadeillas, Degradation of NO using photocatalytic coatings applied to different substrates, Build. Environ. 46(9) (2011) 1808-1816.
[80] M. Faraldos, R. Kropp, M.A. Anderson, K. Sobolev, Photocatalytic hydrophobic concrete coatings to combat air pollution, Catal. Today 259 (2015) 228-236.

[81] J. Chen, C.-s. Poon, Photocatalytic cementitious materials: influence of the microstructure of cement paste on photocatalytic pollution degradation, Environ. Sci. Technol. 43(23) (2009) 8948-8952.
[82] D. Macphee, A. Folli, Photocatalytic concretes—The interface between photocatalysis and cement chemistry, Cem. Concr. Res. 85 (2016) 48-54.
[83] L. Yang, F. Wang, C. Shu, P. Liu, W. Zhang, S. Hu, L. Yang, F. Wang, C. Shu, P. Liu, TiO2/porous cementitious composites: Influences of porosities and TiO2 loading levels on photocatalytic degradation of gaseous benzene, Constr. Build. Mater. 150 (2017) 774-780.
[84] R. Sugrañez, J. Álvarez, M. Cruz-Yusta, I. Mármol, J. Morales, J. Vila, L. Sánchez, Enhanced photocatalytic degradation of NOx gases by regulating the microstructure of mortar cement modified with titanium dioxide, Build. Environ. 69 (2013) 55-63.
[85] S. Karapati, T. Giannakopoulou, N. Todorova, N. Boukos, D. Dimotikali, C. Trapalis, Eco-efficient TiO2 modification for air pollutants oxidation, Appl. Catal., B 176 (2015) 578-585.
[86] F. Wang, Y. Lu, W. Hao, H. Yu, Facile preparation of photocatalytic exposed aggregate concrete with highly efficient and stable catalytic performance, Chem. Eng. J. 264 (2015) 577-586.
[87] L. Yang, A. Hakki, L. Zheng, M.R. Jones, F. Wang, D.E. Macphee, Photocatalytic concrete for NOx abatement: Supported TiO2 efficiencies and impacts, Cem. Concr. Res. 116 (2019) 57-64.
[88] L. Yang, A. Hakki, F. Wang, D.E. Macphee, Photocatalyst efficiencies in concrete technology: The effect of photocatalyst placement, Appl. Catal. B 222 (2018) 200-208.
[89] M.-Z. Guo, J.-S. Li, C.S. Poon, Improved photocatalytic nitrogen oxides removal using recycled glass-nano-TiO2 composites with NaOH pre-treatment, J. Clean. Prod. 209 (2019) 1095-1104.
[90] Z. Du, F. Wang, L. Peng, Y. Lu, W. Zhang, Preparation, Physicochemical Properties, and Long-Term Performance of Photocatalytic Ceramsite Sand in Cementitious Materials, Appl. Sci. 7(8) (2017) 828.
[91] K. Chaidachatorn, J. Suebsuk, S. Horpibulsuk, A. Arulrajah, Extended water/cement ratio law for cement mortar containing recycled asphalt pavement, Constr. Build. Mater. 196 (2019) 457-467.
[92] J. Lin, L. Huo, F. Xu, Y. Xiao, J. Hong, Development of microstructure and early-stage strength for 100% cold recycled asphalt mixture treated with emulsion and cement, Constr. Build. Mater. 189 (2018) 924-933.
[93] H. Wang, R. Zhang, Y. Chen, Z. You, J. Fang, Study on microstructure of rubberized recycled hot mix asphalt based X-ray CT technology, Constr. Build. Mater. 121 (2016) 177-184.
[94] L.P. Abreu, J.R. Oliveira, H.M. Silva, P.V. Fonseca, Recycled asphalt mixtures produced with high percentage of different waste materials, Constr. Build. Mater. 84 (2015) 230-238.
[95] M. Zaumanis, R.B. Mallick, Review of very high-content reclaimed asphalt use in plant-produced pavements: state of the art, Int. J. Pav. Eng. 16(1) (2015) 39-55.
[96] B. Yu, X. Gu, M. Wu, F. Ni, Application of a high percentage of reclaimed asphalt pavement in an asphalt mixture: blending process and performance investigation, Road Mater. Pav. Design 18(3) (2017) 753-765.

[97] X. Lu, K. Xu, P. Chen, K. Jia, S. Liu, C. Wu, Facile one step method realizing scalable production of g-C3N4 nanosheets and study of their photocatalytic H2 evolution activity, J. Mater. Chem. A 2(44) (2014) 18924-18928.
[98] D.M. Holmes, R. Vasant Kumar, W.J. Clegg, Cracking during lateral drying of alumina suspensions, J. Am. Ceram. Soc. 89(6) (2006) 1908-1913.
[99] A. Maury-Ramirez, K. Demeestere, N. De Belie, Photocatalytic activity of titanium dioxide nanoparticle coatings applied on autoclaved aerated concrete: effect of weathering on coating physical characteristics and gaseous toluene removal, J. Hazard. Mater. 211 (2012) 218-225.
[100] A. Chabas, J.-P. Sizun, L. Gentaz, P. Uring, A. Phan, A. Coman, S.C. Alfaro, M. Saheb, E. Pangui, P. Zapf, Water content of limestones submitted to realistic wet deposition: a CIME2 chamber simulation, Environ. Sci. Pollut. Res. 25(24) (2018) 23973-23985.
[101] S. Veltri, A.M. Palermo, G. De Filpo, F. Xu, Subsurface treatment of TiO2 nanoparticles for limestone: Prolonged surface photocatalytic biocidal activities, Build. Environ. 149 (2019) 655-661.
[102] T. Di, B. Zhu, B. Cheng, J. Yu, J. Xu, A direct Z-scheme g-C3N4/SnS2 photocatalyst with superior visible-light CO2 reduction performance, J. Catal. 352 (2017) 532-541.
[103] R. Ghabchi, D. Singh, M. Zaman, Evaluation of moisture susceptibility of asphalt mixes containing RAP and different types of aggregates and asphalt binders using the surface free energy method, Constr. Build. Mater. 73 (2014) 479-489.
[104] Y. Wang, L. Li, Y. Wei, J. Xue, H. Chen, L. Ding, J. Caro, H. Wang, Water Transport with Ultralow Friction through Partially Exfoliated g-C3N4 Nanosheet Membranes with Self-Supporting Spacers, Angew. Chem. Int. Ed. 56(31) (2017) 8974-8980.
[105] L. Chen, Y. Si, Z. Guo, W. Liu, Superhydrophobic sand: a hope for desert water storage and transportation projects, J. Mater. Chem. A 5(14) (2017) 6416-6423.
[106] M. Estevez, Use of coupling agents to stabilize asphalt–rubber–gravel composite to improve its mechanical properties, J. Clean. Prod. 17(15) (2009) 1359-1362.
[107] M.J. Hanus, A.T. Harris, Nanotechnology innovations for the construction industry, Prog. Mater Sci. 58(7) (2013) 1056-1102.
[108] A. Calia, M. Lettieri, M. Masieri, S. Pal, A. Licciulli, V. Arima, Limestones coated with photocatalytic TiO2 to enhance building surface with self-cleaning and depolluting abilities, J. Clean. Prod. 165 (2017) 1036-1047.
[109] T. Adachi, S.S. Latthe, S.W. Gosavi, N. Roy, N. Suzuki, H. Ikari, K. Kato, K.-i. Katsumata, K. Nakata, M. Furudate, Photocatalytic, superhydrophilic, self-cleaning TiO2 coating on cheap, light-weight, flexible polycarbonate substrates, Appl. Surf. Sci. 458 (2018) 917-923.
[110] E. Boonen, A. Beeldens, I. Dirkx, V. Bams, Durability of cementitious photocatalytic building materials, Catal. Today 287 (2017) 196-202.
[111] M.-Z. Guo, C.S. Poon, Superior photocatalytic NOx removal of cementitious materials prepared with white cement over ordinary Portland cement and the underlying mechanisms, Cem. Concr. Compos. 90 (2018) 42-49.

[112] S. Veltri, A.M. Palermo, G. De Filpo, F. Xu, Subsurface treatment of TiO2 nanoparticles for limestone: Prolonged surface photocatalytic biocidal activities, Build. Environ. 149 (2019) 655-661.
[113] G.B. Goffredo, S. Accoroni, C. Totti, T. Romagnoli, L. Valentini, P. Munafo, Titanium dioxide based nanotreatments to inhibit microalgal fouling on building stone surfaces, Build. Environ. 112 (2017) 209-222.
[114] J. de OB Lira, N. Padoin, V.J. Vilar, C. Soares, Photocatalytic NOx abatement: Mathematical modeling, CFD validation and reactor analysis, J. Hazard. Mater. 372 (2019) 145-153.
[115] J. Lasek, Y.-H. Yu, J.C. Wu, Removal of NOx by photocatalytic processes, J. Photoch. Photobio. C 14 (2013) 29-52.
[116] M. Pérez-Nicolás, I. Navarro-Blasco, J.M. Fernández, J.I. Alvarez, Atmospheric NOx removal: study of cement mortars with iron-and vanadium-doped TiO2 as visible light–sensitive photocatalysts, Constr. Build. Mater. 149 (2017) 257-271.
[117] A. Gandolfo, V. Bartolomei, E.G. Alvarez, S. Tlili, S. Gligorovski, J. Kleffmann, H. Wortham, The effectiveness of indoor photocatalytic paints on NOx and HONO levels, Appl. Catal. B: Environ. 166 (2015) 84-90.
[118] Y. Huang, D. Zhu, Q. Zhang, Y. Zhang, J.-j. Cao, Z. Shen, W. Ho, S.C. Lee, Synthesis of a Bi2O2CO3/ZnFe2O4 heterojunction with enhanced photocatalytic activity for visible light irradiation-induced NO removal, Appl. Catal. B: Environ. 234 (2018) 70-78.
[119] Y. Li, W. Ho, K. Lv, B. Zhu, S.C. Lee, Carbon vacancy-induced enhancement of the visible light-driven photocatalytic oxidation of NO over g-C3N4 nanosheets, Appl. Surf. Sci. 430 (2018) 380-389.
[120] J. Zhao, X. Yang, Photocatalytic oxidation for indoor air purification: a literature review, Build. Environ. 38(5) (2003) 645-654.
[121] F. Gauvin, V. Caprai, Q. Yu, H. Brouwers, Effect of the morphology and pore structure of porous building materials on photocatalytic oxidation of air pollutants, Appl. Catal. B: Environ. 227 (2018) 123-131.
[122] D. Fan, C. Guo, H. Ma, D. Zhao, Y. Li, D. Wu, Q. Wei, Facile fabrication of an aptasensor for thrombin based on graphitic carbon nitride/TiO2 with high visible-light photoelectrochemical activity, Biosens. Bioelectron. 75 (2016) 116-122.
[123] Y. Ling, G. Liao, Y. Xie, J. Yin, J. Huang, W. Feng, L. Li, Coupling photocatalysis with ozonation for enhanced degradation of Atenolol by Ag-TiO2 micro-tube, J. Photoch. Photobio. A. 329 (2016) 280-286.
[124] T. Yang, J. Peng, Y. Zheng, X. He, Y. Hou, L. Wu, X. Fu, Enhanced photocatalytic ozonation degradation of organic pollutants by ZnO modified TiO2 nanocomposites, Appl. Catal. B: Environ. 221 (2018) 223-234.
[125] W.-J. Ong, L.-L. Tan, Y.H. Ng, S.-T. Yong, S.-P. Chai, Graphitic carbon nitride (g-C3N4)-based photocatalysts for artificial photosynthesis and environmental remediation: are we a step closer to achieving sustainability, Chem. Rev. 116(12) (2016) 7159-7329.
[126] X. Lu, K. Xu, P. Chen, K. Jia, S. Liu, C. Wu, Facile one step method realizing scalable production of gC 3 N 4 nanosheets and study of their photocatalytic H 2 evolution activity, J. Mater. Chem. A 2(44) (2014) 18924-18928.
[127] J. Wen, J. Xie, X. Chen, X. Li, A review on g-C3N4-based photocatalysts, Appl. Surf. Sci. 391 (2017) 72-123.

[128] G. Mamba, A. Mishra, Graphitic carbon nitride (g-C3N4) nanocomposites: a new and exciting generation of visible light driven photocatalysts for environmental pollution remediation, Appl. Catal. B: Environ. 198 (2016) 347-377.
[129] I. Papailias, T. Giannakopoulou, N. Todorova, D. Demotikali, T. Vaimakis, C. Trapalis, Effect of processing temperature on structure and photocatalytic properties of g-C3N4, Appl. Surf. Sci. 358 (2015) 278-286.
[130] M. Pérez-Nicolás, J. Balbuena, M. Cruz-Yusta, L. Sánchez, I. Navarro-Blasco, J. Fernández, J. Alvarez, Photocatalytic NOx abatement by calcium aluminate cements modified with TiO2: Improved NO2 conversion, Cem. Concr. Res. 70 (2015) 67-76.
[131] M.-Z. Guo, T.-C. Ling, C.S. Poon, Photocatalytic NOx degradation of concrete surface layers intermixed and spray-coated with nano-TiO2: Influence of experimental factors, Cem. Concr. Compos. 83 (2017) 279-289.
[132] M. Faraldos, R. Kropp, M. Anderson, K. Sobolev, Photocatalytic hydrophobic concrete coatings to combat air pollution, Catal. Today 259 (2016) 228-236.
[133] M. Lettieri, D. Colangiuli, M. Masieri, A. Calia, Field performances of nanosized TiO2 coated limestone for a self-cleaning building surface in an urban environment, Build. Environ. 147 (2019) 506-516.
[134] Q. Li, Q. Liu, B. Peng, L. Chai, H. Liu, Self-cleaning performance of TiO2-coating cement materials prepared based on solidification/stabilization of electrolytic manganese residue, Constr. Build. Mater. 106 (2016) 236-242.
[135] B. Jalvo, M. Faraldos, A. Bahamonde, R. Rosal, Antibacterial surfaces prepared by electrospray coating of photocatalytic nanoparticles, Chem. Eng. J. 334 (2018) 1108-1118.
[136] M.M. Hassan, H. Dylla, L.N. Mohammad, T. Rupnow, Evaluation of the durability of titanium dioxide photocatalyst coating for concrete pavement, Constr. Build. Mater. 24(8) (2010) 1456-1461.
[137] N. Bossa, P. Chaurand, C. Levard, D. Borschneck, H. Miche, J. Vicente, C. Geantet, O. Aguerre-Chariol, F.M. Michel, J. Rose, Environmental exposure to TiO2 nanomaterials incorporated in building material, Environ. Pollut. 220 (2017) 1160-1170.
[138] S.A. Diamond, A.J. Kennedy, N.L. Melby, R.D. Moser, A. Poda, C. Weiss Jr, J. Brame, Assessment of the potential hazard of nano-scale TiO2 in photocatalytic cement: application of a tiered assessment framework, NanoImpact 8 (2017) 11-19.
[139] A. Maury-Ramirez, K. Demeestere, N. De Belie, Photocatalytic activity of titanium dioxide nanoparticle coatings applied on autoclaved aerated concrete: effect of weathering on coating physical characteristics and gaseous toluene removal, J. Hazard. Mater. 211 (2012) 218-225.
[140] A.M. Ramirez, K. Demeestere, N. De Belie, T. Mäntylä, E. Levänen, Titanium dioxide coated cementitious materials for air purifying purposes: preparation, characterization and toluene removal potential, Build. Environ. 45(4) (2010) 832-838.
[141] J. Olabarrieta, S. Zorita, I. Peña, N. Rioja, O. Monzón, P. Benguria, L. Scifo, Aging of photocatalytic coatings under a water flow: long run performance and TiO2 nanoparticles release, Appl. Catal. B: Environ. 123 (2012) 182-192.
[142] D.B. Warheit, C.M. Sayes, K.L. Reed, K.A. Swain, Health effects related to nanoparticle exposures: environmental, health and safety considerations for assessing hazards and risks, Pharmacol. Therapeut. 120(1) (2008) 35-42.

[143] K. Inoue, H. Takano, M. Ohnuki, R. Yanagisawa, M. Sakurai, A. Shimada, K. Mizushima, T. Yoshikawa, Size effects of nanomaterials on lung inflammation and coagulatory disturbance, Int. J. immunopath. Ph. 21(1) (2008) 197-206.
[144] T. Verdier, A. Bertron, B. Erable, C. Roques, Bacterial biofilm characterization and microscopic evaluation of the antibacterial properties of a photocatalytic coating protecting building material, Coatings 8(3) (2018) 93.
[145] S.S. Alias, Z. Harun, I.S.A. Latif, Characterization and performance of porous photocatalytic ceramic membranes coated with TiO 2 via different dip-coating routes, J. Mater. Sci. 53(16) (2018) 11534-11552.
[146] D. Colangiuli, A. Calia, N. Bianco, Novel multifunctional coatings with photocatalytic and hydrophobic properties for the preservation of the stone building heritage, Constr. Build. Mater. 93 (2015) 189-196.
[147] S.H. Cho, S.R.White, P.V. Braun, Self‐healing polymer coatings. Adv. Mater. 21(6) (2009):645-649.
[148] M.F. La Russa, N. Rovella, M.A. de Buergo, C.M. Belfiore, A. Pezzino, G.M. Crisci, S.A. Ruffolo, Nano-TiO2 coatings for cultural heritage protection: The role of the binder on hydrophobic and self-cleaning efficacy, Prog. Org. Coat. 91 (2016) 1-8.
[149] M.F. La Russa, S.A. Ruffolo, N. Rovella, C.M. Belfiore, A.M. Palermo, M.T. Guzzi, G.M. Crisci, Multifunctional TiO2 coatings for cultural heritage, Prog. Org. Coat. 74(1) (2012) 186-191.
[150] F. Persico, M. Sansotera, C.L. Bianchi, C. Cavallotti, W. Navarrini, Photocatalytic activity of TiO2-embedded fluorinated transparent coating for oxidation of hydrosoluble pollutants in turbid suspensions, Appl. Catal. B: Environ. 170 (2015) 83-89.
[151] C. Mendoza, A. Valle, M. Castellote, A. Bahamonde, M. Faraldos, TiO2 and TiO2–SiO2 coated cement: Comparison of mechanic and photocatalytic properties, Appl. Catal. B: Environ. 178 (2015) 155-164.
[152] F. Pino, P. Fermo, M. La Russa, S. Ruffolo, V. Comite, J. Baghdachi, E. Pecchioni, F. Fratini, G. Cappelletti, Advanced mortar coatings for cultural heritage protection. Durability towards prolonged UV and outdoor exposure, Environ. Sci. and Pollut. R. 24(14) (2017) 12608-12617.
[153] P. Carmona-Quiroga, S. Martínez-Ramírez, H. Viles, Efficiency and durability of a self-cleaning coating on concrete and stones under both natural and artificial ageing trials, Appl. Surf. Sci. 433 (2018) 312-320.
[154] Y. Zhang, J. Liu, G. Wu, W. Chen, Porous graphitic carbon nitride synthesized via direct polymerization of urea for efficient sunlight-driven photocatalytic hydrogen production, Nanoscale 4(17) (2012) 5300-5303.
[155] M. Drdácký, J. Lesák, S. Rescic, Z. Slížková, P. Tiano, J. Valach, Standardization of peeling tests for assessing the cohesion and consolidation characteristics of historic stone surfaces, Mater. Struct. 45(4) (2012) 505-520.
[156] A. Calia, M. Lettieri, M. Masieri, Durability assessment of nanostructured TiO2 coatings applied on limestones to enhance building surface with self-cleaning ability, Build. Environ. 110 (2016) 1-10.
[157] M.-Z. Guo, J.-S. Li, C.S. Poon, Improved photocatalytic nitrogen oxides removal using recycled glass-nano-TiO2 composites with NaOH pre-treatment, J. Clean. Prod. 209 (2019) 1095-1104.

[158] Y. Yang, T. Ji, W. Su, B. Yang, Y. Zhang, Z. Yang, Photocatalytic NOx abatement and self-cleaning performance of cementitious composites with g-C3N4 nanosheets under visible light, Constr. Build. Mater. 225 (2019) 120-131.
[159] V.K. Yemmireddy, G.D. Farrell, Y.C. Hung, Development of titanium dioxide (TiO2) nanocoatings on food contact surfaces and method to evaluate their durability and photocatalytic bactericidal property, J. Food Sci. 80(8) (2015) N1903-N1911.
[160] D. Colangiuli, M. Lettieri, M. Masieri, A. Calia, Field study in an urban environment of simultaneous self-cleaning and hydrophobic nanosized TiO2-based coatings on stone for the protection of building surface, Sci. Total Environ. 650 (2019) 2919-2930.
[161] I. Alfieri, A. Lorenzi, L. Ranzenigo, L. Lazzarini, G. Predieri, P.P. Lottici, Synthesis and characterization of photocatalytic hydrophobic hybrid TiO2-SiO2 coatings for building applications, Build. Environ. 111 (2017) 72-79.
[162] G. Jiang, J. Cao, M. Chen, X. Zhang, F. Dong, Photocatalytic NO oxidation on N-doped TiO2/g-C3N4 heterojunction: Enhanced efficiency, mechanism and reaction pathway, Appl. Surf. Sci. 458 (2018) 77-85.
[163] T. Martinez, A. Bertron, E. Ringot, G. Escadeillas, Degradation of NO using photocatalytic coatings applied to different substrates, Build. Environ. 46(9) (2011) 1808-1816.
[164] P. Munafo, G.B. Goffredo, E. Quagliarini, TiO2-based nanocoatings for preserving architectural stone surfaces: An overview, Constr. Build. Mater. 84 (2015) 201-218.
[165] M.V. Diamanti, R. Paolini, M. Rossini, A.B. Aslan, M. Zinzi, T. Poli, M.P. Pedeferri, Long term self-cleaning and photocatalytic performance of anatase added mortars exposed to the urban environment, Constr. Build. Mater. 96 (2015) 270-278.
[166] C. Sciancalepore, F. Bondioli, Durability of SiO2–TiO2 photocatalytic coatings on ceramic tiles, Int. J. Appl. Ceram. Tec. 12(3) (2015) 679-684.
[167] P. Krishnan, M.-H. Zhang, L. Yu, H. Feng, Photocatalytic degradation of particulate pollutants and self-cleaning performance of TiO2-containing silicate coating and mortar, Constr. Build. Mater. 44 (2013) 309-316.